THESIS FOR THE DEGREE OF DOCTOR OF PHILOSOPHY

Single Base Station mmWave Radio Positioning, Mapping, and SLAM

Yu Ge

CHALMERS
UNIVERSITY OF TECHNOLOGY

Communication Systems Group
Department of Electrical Engineering
Chalmers University of Technology
Gothenburg, Sweden, 2024

Single Base Station mmWave Radio Positioning, Mapping, and SLAM

Yu Ge

ISBN 978-91-8103-019-8
Ny series No. 5477
Doktorsavhandlingar vid Chalmers tekniska högskola
ISSN 0346-718X

This thesis has been prepared using LaTeX and Tikz.

Communication Systems Group
Department of Electrical Engineering
Chalmers University of Technology
SE-412 96 Gothenburg, Sweden
Phone: +46 (0)31 772 1000
www.chalmers.se

Front cover illustration:
A single base station 5G mmWave downlink scenario with two landmarks, where signals sent from the base station can reach the user equipment via the line-of-sight (the black line) and none-line-of-sight (red lines) paths.

Printed by Chalmers Reproservice
Gothenburg, Sweden, February 2024

Single Base Station mmWave Radio Positioning, Mapping, and SLAM

Yu Ge
Department of Electrical Engineering
Chalmers University of Technology

Abstract

Fifth-generation (5G) communication systems in Frequency Range 2, operating above 24 GHz and utilizing mmWave signals, showcase distinct properties that open up new possibilities in positioning, mapping, and simultaneous localization and mapping (SLAM). The combination of large bandwidth, extensive antenna arrays, and high carrier frequency results in geometric-based signals, and unprecedented delay and angle resolution. These enable the system to resolve multipath components, providing high-accuracy geometric information among the user equipment (UE), the base station (BS), and the environment. These high-accuracy geometric information allows for highly accurate UE positioning, environment mapping, and SLAM, all achievable using a single BS.

While numerous studies have delved into the single BS positioning and mapping problem using snapshot measurements, a significant portion of them remains confined to theoretical analyses with many simplified assumptions. Real-world experimental validation is scarce, particularly in scenarios involving a commercial 5G BS. Additionally, while diffuse multipath contains valuable geometric information, it is often treated as a perturbation or fails to acknowledge that diffuse multipath signals may originate from the same source landmark, leading to information loss. When extending positioning and mapping to a SLAM problem by tracking the UE over time, a radio SLAM problem emerges, posing the primary challenge of effectively addressing the data association (DA) problem. It is these research gaps and challenges that drive the motivation behind this thesis.

Within this thesis, [Paper A] and [Paper B] address the radio SLAM problem, with [Paper A] additionally exploring the utilization of diffuse multipath. In [Paper A], we adopt an end-to-end approach to address the radio SLAM problem, presenting a comprehensive framework for SLAM. This includes the introduction of a random finite set (RFS)-based SLAM filter designed to overcome the DA challenge inherent in radio SLAM, along with a method to effectively leverage all paths originating from the same landmark. Meanwhile, an efficient alternative RFS-based SLAM filter, designed for real-time implementation, is proposed in [Paper B] as a counterpart to the solution presented in [Paper A]. In [Paper C], we focus on experimental validation of positioning and mapping with a single BS, showcasing the practical feasibility while uncovering existing gaps between theoretical expectations and real-world implementation. [Paper D] delves into the fusion problem involving mapping and SLAM results from various sources, presenting an RFS-based fusion solution.

Keywords: 5G, mmWave, positioning, mapping, SLAM, single BS, experimental validation, diffuse multipath, DA, RFS, fusion.

List of Publications

This thesis is based on the following publications:

[A] **Y. Ge**, F. Wen, H. Kim, M. Zhu, F. Jiang, S. Kim, L. Svensson, and H. Wymeersch, "5G SLAM using the clustering and assignment approach with diffuse multipath," *Sensors (Basel, Switzerland)*, vol. 20, no. 16, August 2020. [Online]. Available: https://doi.org/10.3390/s20164656.

[B] **Y. Ge**, O. Kaltiokallio, H. Kim, F. Jiang, J. Talvitie, M. Valkama, L. Svensson, S. Kim, and H. Wymeersch, "A computationally efficient EK-PMBM filter for bistatic mmWave radio SLAM," *IEEE Journal on Selected Areas in Communications*, vol. 40, no. 7, pp. 2179-2192, July 2022, doi: 10.1109/JSAC.2022.3155504.

[C] **Y. Ge**, H. Khosravi, F. Jiang, H. Chen, S. Lindberg, P. Hammarberg, H. Kim, O. Brunnegård, O. Eriksson, B. Olsson, F. Tufvesson, L. Svensson, and H. Wymeersch, "Experimental validation of single BS 5G mmWave positioning and mapping for intelligent transport," submitted to *IEEE Transactions on Vehicular Technology*, 2023.

[D] **Y. Ge**, H. Kim, L. Svensson, H. Wymeersch, and S. Sun, "Integrated monostatic and bistatic mmWave sensing," in *IEEE Global Communications Conference*, Kuala Lumpur, Malaysia, December 2023.

Publications by the author not included in the thesis:

[E] **Y. Ge**, M. Stark, M. Keskin, F. Hofmann, T. Hansen, and H. Wymeersch, "V2X sidelink positioning in FR1: Scenarios, algorithms, and performance evaluation," submitted to *IEEE Journal on Selected Areas in Communications*, 2023.

[F] **Y. Ge**, O. Kaltiokallio, H. Kim, J. Talvitie, S. Kim, L. Svensson, M. Valkama, and H. Wymeersch, "MmWave mapping and SLAM for 5G and beyond", in *Integrated Sensing and Communications (ISAC)*, Springer Nature Singapore, 2023. 445-475.

[G] **Y. Ge**, M. Stark, M. Keskin, F. Hofmann, T. Hansen, and H. Wymeersch, "Analysis of V2X sidelink positioning in sub-6 GHz," in *IEEE International Symposium on Joint Communications & Sensing (JC&S)*, Seefeld, Austria, 2023, pp. 1-6, doi: 10.1109/JCS57290.2023.10107458.

[H] **Y. Ge**, O. Kaltiokallio, H. Chen, F. Jiang, J. Talvitie, M. Valkama, L. Svensson, and H. Wymeersch, "Doppler exploitation in bistatic mmWave radio SLAM," in *IEEE Global Communications Conference*, Rio de Janeiro, Brazil, 2022, pp. 6463-6468, doi: 10.1109/GLOBECOM48099.2022.10001597.

[I] **Y. Ge**, H. Chen, F. Jiang, M. Zhu, H. Khosravi, S. Lindberg, H. Herbertsson, O. Eriksson, O. Brunnegard, B. Olsson, P. Hammarberg, F. Tufvesson, L. Svensson, and H. Wymeersch, "Experimental validation of single base station 5G mmWave positioning: Initial findings," in *International Conference on Information Fusion (FUSION)*, Linköping, Sweden, 2022, pp. 1-8, doi: 10.23919/FUSION49751.2022.9841230.

[J] **Y. Ge**, Y. Wu, F. Jiang, O. Kaltiokallio, J. Talvitie, M. Valkama, L. Svensson, and H. Wymeersch, "Iterated posterior linearization PMB filter for 5G SLAM," in *IEEE International Conference on Communications*, Seoul, Republic of Korea, 2022, pp. 877-882, doi: 10.1109/ICC45855.2022.9839281.

[K] **Y. Ge**, F. Jiang, M. Zhu, F. Wen, L. Svensson, and H. Wymeersch, "5G SLAM with low-complexity channel estimation," in *European Conference on Antennas and Propagation (EuCAP)*, Dusseldorf, Germany, 2021, pp. 1-5, doi: 10.23919/EuCAP51087.2021.9411339.

[L] **Y. Ge**, H. Kim, F. Wen, L. Svensson, S. Kim, and H. Wymeersch, "Exploiting diffuse multipath in 5G SLAM," in *IEEE Global Communications Conference*, Taipei, Taiwan, 2020, pp. 1-6, doi: 10.1109/GLOBECOM42002.2020.9322120.

[M] H. Chen, P. Zheng, **Y. Ge**, A. Elzanaty, J. He, T. Al-Naffouri, and H. Wymeersch, "ELAA near-field localization and sensing with partial blockage detection," submitted to *IEEE International Symposium on Personal, Indoor and Mobile Radio Communications*, Valencia, Spain, 2024.

[N] O. Kaltiokallio, R. Hostettler, **Y. Ge**, H. Kim, J. Talvitie, H. Wymeersch, and M. Valkama, "A multi-hypotheses importance density for SLAM in cluttered scenarios," *IEEE Transactions on Robotics*, December 2023.

[O] E. Rastorgueva-Foi, O. Kaltiokallio, **Y. Ge**, M. Turunen, J. Talvitie, B. Tan, M. Keskin, H. Wymeersch, and M. Valkama, "Millimeter-wave radio SLAM: End-to-end processing methods and experimental validation," submitted to *IEEE Journal on Selected Areas in Communications*, 2023.

[P] H. Chen, H. Kim, R. Ghazalian, C. Ozturk, M. Ammous, **Y. Ge**, M. Keskin, S. Gezici, S. Valaee, and H. Wymeersch, "Calibration in RIS-aided localization systems," submitted to *Calibration in RIS-aided Localization Systems*, Springer Nature Singapore, 2023.

[Q] H. Kim, Á. García-Fernández, **Y. Ge**, Y. Xia, L. Svensson, and H. Wymeersch, "Set-type belief propagation with applications to mapping, MTT, SLAM, and SLAT," submitted to *IEEE Transactions on Signal Processing*, 2023.

[R] H. Kim, H. Chen, M. Keskin, **Y. Ge**, K. Keykhosravi, G. Alexandropoulos, S. Kim, and H. Wymeersch, "RIS-enabled and access-point-free simultaneous radio localization and mapping," *IEEE Transactions on Wireless Communications*, August 2023, doi: 10.1109/TWC.2023.3307455.

[S] H. Kim, A. Fascista, H. Chen, **Y. Ge**, G. Alexandropoulos, G. Seco-Granadosand, and H. Wymeersch, "RIS-aided radar sensing and object detection with single and double bounce multipath," in *IEEE International Conference on Communications Workshops (ICC Workshops)*, Rome, Italy, 2023, pp. 1883-1889, doi: 10.1109/ICCWorkshops57953.2023.10283494.

[T] O. Kaltiokallio, J. Talvitie, **Y. Ge**, H. Wymeersch, and M. Valkama, "Estimating initial map features for improving consistency of 5G SLAM," in *IEEE International Conference on Communications Workshops (ICC Workshops)*, Rome, Italy, 2023, pp. 1641-1647, doi: 10.1109/ICCWorkshops57953.2023.10283708.

[U] F. Jiang, **Y. Ge**, M. Zhu, H. Wymeersch, and F. Tufvesson, "Low-complexity channel estimation and localization with random beamspace observations," in *IEEE International Conference on Communications*, Rome, Italy, 2023, pp. 5985-5990, doi: 10.1109/ICC45041.2023.10278994.

[V] H. Chen, F. Jiang, **Y. Ge**, H. Kim, and H. Wymeersch, "Doppler-enabled single-antenna localization and mapping without synchronization," in *IEEE Global Communications Conference*, Rio de Janeiro, Brazil, 2022, pp. 6469-6474, doi: 10.1109/GLOBECOM48099.2022.10001351.

[W] H. Kim, J. Lee, **Y. Ge**, F. Jiang, S. Kim and H. Wymeersch, "Cooperative mmWave PHD-SLAM with moving scatterers," in *International Conference on Information Fusion (FUSION)*, Linköping, Sweden, 2022, pp. 1-6, doi: 10.23919/FUSION49751.2022.9841389.

[X] O. Kaltiokallio, R. Hostettle, J. Talvitie, **Y. Ge**, H. Kim, H. Wymeersch, and M. Valkama, "Towards real-time radio-SLAM via optimal importance sampling," in *IEEE International Workshop on Signal Processing Advances in Wireless Communication (SPAWC)*, Oulu, Finland, 2022, pp. 1-5, doi: 10.1109/SPAWC51304.2022.9833982.

[Y] O. Kaltiokallio, J. Talvitie, **Y. Ge**, H. Wymeersch, and M. Valkama, "MmWave mapping using PHD with smoothed track confirmation and multi-bounce suppression," in *IEEE International Conference on Communications Workshops (ICC Workshops)*, Seoul, Republic of Korea, 2022, pp. 67-72, doi: 10.1109/ICCWorkshops53468.2022.9814587.

[Z] O. Kaltiokallio, **Y. Ge**, J. Talvitie, H. Wymeersch, and M. Valkama, "MmWave simultaneous localization and mapping using a computationally efficient EK-PHD

filter," in *IEEE International Conference on Information Fusion (FUSION)*, Sun City, South Africa, 2021, pp. 1-8, doi: 10.23919/FUSION49465.2021.9626927.

[i] F. Jiang, F. Wen, **Y. Ge**, M. Zhu, H. Wymeersch, and F. Tufvesson, "Beamspace multidimensional ESPRIT approaches for simultaneous localization and communications," *arXiv preprint arXiv:2111.07450*, 2021.

[ii] F. Jiang, **Y. Ge**, M. Zhu, and H. Wymeersch, "High-dimensional channel estimation for simultaneous localization and communications," in *IEEE Wireless Communications and Networking Conference (WCNC)*, Nanjing, China, 2021, pp. 1-6, doi: 10.1109/WCNC49053.2021.9417496.

Acknowledgements

Finalizing my PhD journey marks not only the culmination of years of dedicated research but also the beginning of an exciting new chapter. I am profoundly grateful for the unwavering support, guidance, and encouragement I have received from the exceptional individuals who have contributed to this significant milestone.

First and foremost, my deepest gratitude goes to my main supervisor and examiner, Prof. Henk Wymeersch. Your dedication, insightful guidance, and constructive feedback have been instrumental in shaping both this thesis and my academic journey. Your mentorship has been a beacon of inspiration, and I feel truly privileged to have had the opportunity to work under your tutelage. Additionally, I wish to express my sincere appreciation to my co-supervisor, Prof. Lennart Svensson. Your expertise, encouragement, and scholarly insights have greatly enriched the depth and quality of my research. I am grateful for the collaborative spirit you have instilled throughout this process.

My heartfelt thanks extend to Prof. Mikko Valkama, Prof. Sumei Sun, Prof. Sunwoo Kim, Prof. Fredrik Tufvesson, Dr. Hyowon Kim, Dr. Ossi Kaltiokallio, Dr. Jukka Talvitie, Dr. Hui Chen, Dr. Musa Furkan Keskin, Dr. Fuxi Wen, Dr. Fan Jiang, Dr. Yuxuan Xia, and Dr. Ángel García-Fernández for generously sharing their knowledge, expertise, resources, and support. Your contributions have broadened my perspective and enriched my research experience. Furthermore, I extend my heartfelt appreciation to all my co-authors for their invaluable contributions to all my publications. Your collaboration, dedication, and expertise have played a pivotal role in advancing our collective understanding in our respective fields.

Special gratitude is due to Dr. Sharief Saleh, Dr. Hyowon Kim, Dr. Yuxuan Xia, Dr. Hao Guo, and Mr. Yibo Wu, who dedicated their time and expertise to proofread and provide constructive feedback on this thesis. Your meticulous attention to detail and insightful suggestions have undoubtedly enhanced the quality of this work.

To my colleagues, I am grateful for your camaraderie, support, and stimulating discussions, which have enriched my academic journey and provided invaluable insights. To my friends, who have been unwavering sources of encouragement, laughter, and support, I am deeply thankful. Your friendship has made this journey all the more rewarding.

Last but certainly not least, I extend my deepest gratitude to my family and the love of my life for their unconditional love, unwavering support, and endless encouragement. Your belief in me has been my greatest motivation, and I am profoundly grateful for your unwavering faith and encouragement.

Yu Ge
Gothenburg, February, 2024

Financial Support

This work was partially supported by the Wallenberg AI, Autonomous Systems and Software Program (WASP) funded by Knut and Alice Wallenberg Foundation, by the Vinnova 5GPOS project under grant 2019-03085, and by Hexa-X-II, part of the European Union's Horizon Europe research and innovation programme under Grant Agreement No. 101095759.

Acronyms

1G:	First-generation
2G:	Second-generation
3G:	Third-generation
4G:	Fourth-generation
5G:	Fifth-generation
6G:	Sixth-generation
AoA:	Angle-of-arrival
AoD:	Angle-of-departure
BP:	Belief propagation
BS:	Base station
DA:	Data association
DBSCAN:	Density-based spatial clustering of applications with noise
EK:	Extended Kalman
EKF:	Extended Kalman filter
ESPRIT:	Estimation of parameters by rotational invariant techniques
FoV:	Field-of-view
FR2:	Frequency Range 2
GNSS:	Global navigation satellite system
GOSPA:	Generalized optimal subpattern assignment
IMU:	Inertial measurement unit

IoT:	Internet of Things
IP:	Incidence point
ISAC:	Integrated sensing and communication
LMB:	Labeled multi-Bernoulli
LoS:	Line-of-sight
MB:	Multi-Bernoulli
MBM:	Multi-Bernoulli mixture
MIMO:	Multiple-input multiple-output
ML:	Maximum likelihood
MOT:	Multi-object tracking
NLoS:	Non-line-of-sight
OFDM:	Orthogonal frequency-division multiplexing
OSPA:	Optimal subpattern assignment
PDF:	Probability density function
PHD:	Probability hypothesis density
PMB:	Poisson multi-Bernoulli
PMBM:	Poisson multi-Bernoulli mixture
PPP:	Poisson point process
RBP:	Rao-Blackwellized particle
RBPF:	Rao-Blackwellized particle filter

RF:	Radio frequency
RFS:	Random finite set
RIS:	Reconfigurable intelligent surface
RTT:	Round-trip-time
SLAM:	Simultaneous localization and mapping
SLAT:	Simultaneous localization and tracking
SP:	Scattering point
TDoA:	Time-difference-of-arrival
ToA:	Time-of-arrival
TOMB/P:	Track-oriented marginal multi-Bernoulli/Poisson
UE:	User equipment
ULA:	Uniform linear array
URA:	Uniform rectangular array
V2X:	Vehicle-to-Everything
VA:	Virtual anchor
δ-GLMB:	δ-generalized labeled multi-Bernoulli

Contents

Part I

Overview

CHAPTER 1

Introduction

1.1 Background

The evolution of wireless communication has witnessed remarkable progress from the first-generation (1G) mobile networks in the 1980s to the recent deployment of fifth-generation (5G) cellular networks, where the first commercial 5G cellular networks were deployed in late 2019, while discussions about the future sixth-generation (6G) networks are underway [1–3], as summarized in Fig. 1.1. This continuous advancement has transformed wireless technologies, offering higher data rates, increased capacity, reduced latency, and more connectivity for diverse applications, making wireless communications and their associated applications become integral aspects of our daily lives.

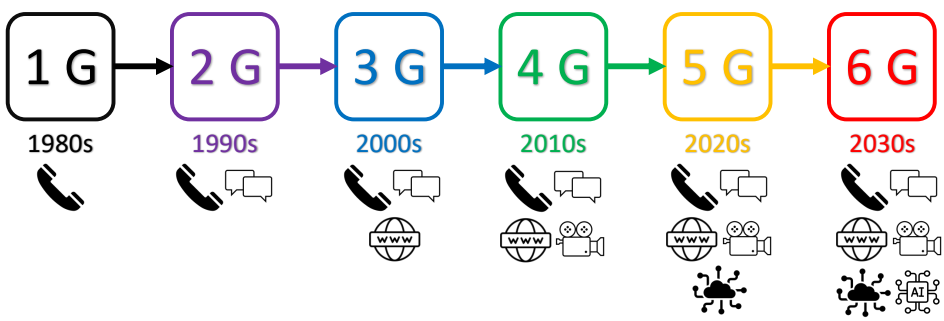

Figure 1.1: Network evolution from 1G to 6G.

Successive generations of cellular communication systems share a common characteristic: each iteration relies on a larger bandwidth and higher carrier frequency than its predecessor. This trend is particularly pronounced in 5G, where carriers above 24 GHz and mmWave signals are employed in Frequency Range 2 (FR2), accompanied by contiguous bandwidths reaching up to 400 MHz and massive multiple-input multiple-output (MIMO) antenna arrays [2, 4]. The escalation in bandwidth, antenna array size, and carrier frequencies results in more geometric-based signals and higher resolutions in both delay and angles [5, 6]. These enhancements extend the potential applications of 5G beyond traditional communication, opening unprecedented avenues for highly accurate positioning, mapping, and simultaneous localization and mapping (SLAM) [7–10]. These capabilities are pivotal in various applications, including autonomous driving [11], Vehicle-to-Everything (V2X) communication [12, 13], spatial signal design [14, 15], integrated sensing and communication (ISAC) [16–19], and numerous other domains.

Specifically, cellular communication infrastructure can function as a supplementary sensor for absolute positioning alongside global navigation satellite system (GNSS), which remains the predominant positioning technology in various applications [20, 21]. While GNSS offers stable and accurate positioning services [22], it encounters limitations in specific scenarios, such as indoors and densely urbanized areas [23, 24]. Notably, reliable cellular network coverage is often assured in these indoor and densely urban settings. Furthermore, sensing and SLAM services leveraging cellular networks can complement the functionalities of other onboard sensors in unmanned vehicles, such as radar, cameras, lidar, and inertial measurement units (IMUs) [25]. This approach is advantageous, as it inherently provides a global reference, and the additional set of observations contributes to an overall performance enhancement. Importantly, these positioning, mapping, and SLAM services emerge as byproducts of communication, eliminating the need for significant dedicated deployments and maintenance costs since they rely on existing communication infrastructure.

Cellular technologies have played a role in positioning for several decades [5,20]. For example, second-generation (2G) communication facilitated cell-ID-based positioning, offering accuracies in the order of a few hundred meters. The incorporation of time-difference-of-arrival (TDoA) measurements in third-generation (3G) improved accuracy to the order of tens of meters, and further enhancements were observed in fourth-generation (4G) with dedicated pilot patterns. However, the positioning performances of these cellular generations have not met the positioning requirements of many applications, leading to limited consideration in various applications.

The advent of 5G mmWave wireless communication systems, with their geometric-based signals and enhanced delay and angle resolutions, has transformed the landscape of cellular positioning [21, 26]. Consequently, extensive research efforts have delved into 5G positioning, prompting dedicated studies within 3GPP. A notable example is the report presented in 3GPP [27], wherein findings underscored the feasibility of meeting commercial positioning performance requirements through the utilization of both delay

and angle measurements. Furthermore, to actualize 5G positioning, 3GPP has embarked on standardization initiatives to accommodate diverse commercial use cases with varying performance prerequisites, as outlined in [28, 29].

In contrast to communication, where a link can be established with a single base station (BS), a notable challenge in 5G mmWave positioning is the substantial infrastructure demand of multiple BSs [30–32]. To mitigate this reliance on infrastructure, the research community has diligently explored alternative approaches. One such approach envisions achieving 3D positioning of a user equipment (UE), potentially including its orientation and synchronization with the BS, with a single BS, eliminating the need for external sensors, additional infrastructure, and additional time-frequency resource costs. The key to its success lies in equipping both UE and BS with uniform rectangular arrays (URAs), and leveraging at least one resolvable multipath component in the environment [7, 33–35]. While significant theoretical progress has been made, only a limited subset of these approaches has demonstrated practical viability [33, 36–38], particularly when implemented with commercial BSs. In light of this, we present a unique real-world demonstration of single BS 5G mmWave positioning for a BS using commercial hardware and an actual vehicle. The results and findings of this demonstration are detailed in [Paper C].

Beyond mere positioning, the sparsity inherent in the mmWave channel at higher carrier frequencies offers a unique advantage—the ability to resolve multipath components, transforming them from adversaries to allies [33, 39]. Specifically, the geometric characteristics of the mmWave channel establish a connection between multipath parameters and the physical environment. These parameters, tied to the UE state in relation to the BS and the propagation environment, can be leveraged in the positioning and mapping problem. By decoding multipath parameters from received signals, one can extract geometric information that not only pinpoints the UE state but also delineates the locations of landmarks in the environment [33]. This challenge becomes even more intricate when integrated with UE tracking, giving rise to the radio SLAM problem [40, 41].

Many papers have harnessed signals from a single BS within a single snapshot to estimate the UE state and conduct mapping in various scenarios, incorporating both line-of-sight (LoS) and non-line-of-sight (NLoS) paths [42–45]. However, the consideration of multiple measurements per object, a common thread in the SLAM and extended object tracking literature, has been relatively overlooked or simplified in existing works. In [Paper A], we introduce a radio SLAM framework capable of harnessing both specular and diffuse multipath from the same landmark.

Generally, the single snapshot positioning and mapping problem poses fewer challenges than the SLAM problem. This distinction arises from the need to address the over-time data association (DA) problem introduced by tracking in SLAM, while snapshot-based DA is the primary concern in positioning and mapping problems [46]. Various solutions to the DA problem exist, ranging from classic linear assignment algorithms seeking the best association to probabilistic methods based on belief propagation (BP) [47, 48] or

random finite set (RFS) theory [49–51]. In [Paper A] and [Paper B], we introduce two versions of RFS-based solutions for radio SLAM based on the Poisson multi-Bernoulli mixture (PMBM) RFS, and [Paper D] addresses the fusion problem of mapping and SLAM results from different sources.

1.2 Thesis scope

This thesis pursues a four-fold objective. Firstly, it serves to introduce the positioning, mapping, and SLAM problems within the realm of mmWave communication, specifically in the context of a single BS downlink scenario. Secondly, the thesis aims to outline the requirements and present general solutions for addressing the snapshot positioning and mapping problem when utilizing a single BS. Thirdly, it endeavors to offer a comprehensive introduction to the fundamentals of RFS theory and delineate how radio SLAM can be effectively addressed at a high level using the RFS theory. Lastly, the thesis provides insights into leveraging multipath signals from a single object in addressing mmWave radio positioning, mapping, and SLAM challenges.

1.3 Thesis outline

This thesis is structured into two parts, each serving a distinct purpose. Part I is dedicated to furnishing essential background knowledge for comprehending the appended papers found in Part II. The papers included in Part II are centered around the design and evaluation of diverse methods addressing radio positioning, mapping, and SLAM challenges within the context of a 5G mmWave single BS downlink scenario featuring a single UE.

The remainder of Part I is structured as follows:

- Chapter 2: Introduces the system models relevant to a typical 5G mmWave single BS downlink scenario.
- Chapter 3: Explores the intricacies of single snapshot radio positioning and mapping, reviews classical positioning methods, and outlines fundamental approaches to solving the single BS positioning and mapping problem.
- Chapter 4: Introduces the radio SLAM problem, and offers insights into existing SLAM solutions in the literature.
- Chapter 5: Covers the fundamental concepts and properties of RFS, along with evaluation metrics.
- Chapter 6: Presents the RFS-SLAM scheme, elucidates the incorporation of radio measurements, outlines implementations, and discusses the fusion of different mapping and SLAM results.

- Chapter 7: Summarizes the contributions made in the appended papers, and discusses potential directions for future research.

1.4 Notations

Scalars (e.g., x) are denoted in italic, vectors (e.g., $\boldsymbol{x}$) in bold, matrices (e.g., $\boldsymbol{X}$) in bold capital letters, sets (e.g., $\mathcal{X}$) in calligraphic, and its cardinality is denoted as $|\mathcal{X}|$. The transpose is denoted by $(\cdot)^\top$. The L2 norm is denoted by $\|\cdot\|$. The i-th component in vector $\boldsymbol{x}$ is denoted by $[\boldsymbol{x}]_i$. The emptyset is denoted by $\varnothing$. The union of mutually disjoint sets is denoted by $\uplus$. A Gaussian density with mean $\boldsymbol{u}$ and covariance $\boldsymbol{C}$, evaluated in value $\boldsymbol{x}$ is denoted by $\mathcal{N}(\boldsymbol{x}; \boldsymbol{u}, \boldsymbol{C})$.

CHAPTER 2

Models of states and measurements

In this thesis, the primary focus is on a 5G mmWave downlink scenario featuring a single BS and a single UE. In this setup, the BS transmits downlink signals to the UE at each time step, as illustrated in Fig. 2.1. This chapter initiates by introducing the state models for the UE, the BS, and landmarks within the considered scenario. Additionally, the measurement model for the mmWave downlink scenario is presented.

2.1 State models

The propagation environment in the examined scenario, shown in Fig. 2.1, encompasses a mobile UE, a fixed BS, and static landmarks. The state models for these entities are elucidated below. It is important to emphasize that the global reference coordinate system serves as the reference framework throughout this thesis.

BS

In a standard radio scenario, the BS remains stationary and is equipped with an antenna array (or a single antenna), having its center located at $\boldsymbol{p}_{\mathrm{BS}} = [x_{\mathrm{BS}}, y_{\mathrm{BS}}, z_{\mathrm{BS}}]^{\mathsf{T}}$. If a URA is employed, the array has an orientation, denoted by $\boldsymbol{\psi}_{\mathrm{BS}} = [\alpha_{\mathrm{BS}}, \beta_{\mathrm{BS}}, \gamma_{\mathrm{BS}}]^{\mathsf{T}}$, representing roll, pitch, and yaw, in the respective order. This orientation signifies the orientation of the transmitter URA with respect to the the reference coordinate system [52]. However, when a uniform linear array (ULA) or a single antenna is utilized, $\boldsymbol{\psi}_{\mathrm{BS}}$ has fewer components, or there is no need to consider $\boldsymbol{\psi}_{\mathrm{BS}}$ at all. Consequently, in the general case, the state of the BS can be expressed as $\boldsymbol{s}_{\mathrm{BS}} = [\boldsymbol{p}_{\mathrm{BS}}^{\mathsf{T}}, \boldsymbol{\psi}_{\mathrm{BS}}^{\mathsf{T}}]^{\mathsf{T}}$, typically known

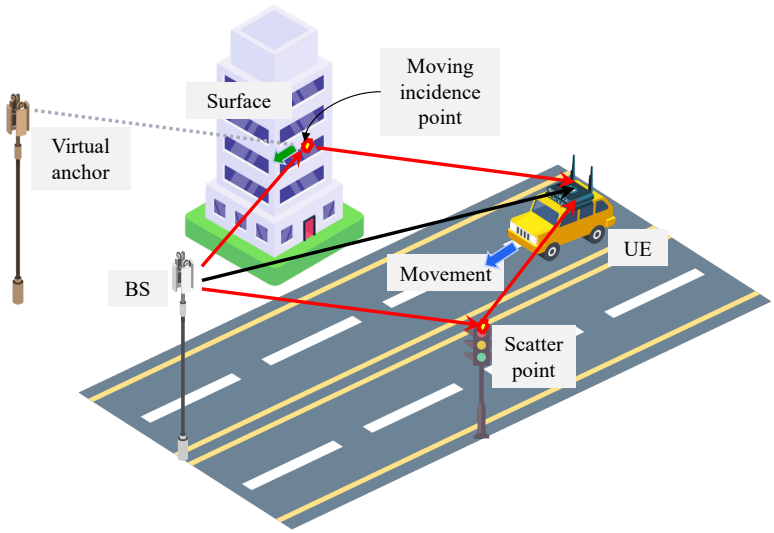

Figure 2.1: A single BS 5G mmWave downlink scenario with a moving UE, and a few landmarks, where signals transmitted from the BS can reach the UE through both the LoS path, depicted by the black line, and NLoS paths, depicted by the red lines.

as a priori.

UE

The UE is capable of dynamic movement and, similarly to the BS, equipped with either an antenna array or a single antenna. For the sake of generalization, we consider a scenario in which the UE is equipped with a URA when describing its state. In addition to considering the parameters of position and orientation, the clock bias resulting from imperfect synchronization between the transmitter and the receiver is also typically taken into account. Consequently, the state of the UE at time step k is denoted as $\boldsymbol{s}_{\mathrm{UE},k} = [\boldsymbol{p}_{\mathrm{UE},k}^{\mathsf{T}}, \boldsymbol{\psi}_{\mathrm{UE},k}^{\mathsf{T}}, b_k]^{\mathsf{T}}$. Here, $\boldsymbol{p}_{\mathrm{UE},k} = [x_{\mathrm{UE},k}, y_{\mathrm{UE},k}, z_{\mathrm{UE},k}]^{\mathsf{T}}$ signifies the position of the center of the URA at the UE side, $\boldsymbol{\psi}_{\mathrm{UE},k} = [\alpha_{\mathrm{UE},k}, \beta_{\mathrm{UE},k}, \gamma_{\mathrm{UE},k}]^{\mathsf{T}}$ indicates the orientation of the receiver, and b_k represents the clock bias between the transmitter and receiver.

As the UE undergoes movement over time, it evolves according to state dynamics, and the transition density is given by

$$f(\boldsymbol{s}_k|\boldsymbol{s}_{k-1}, \boldsymbol{u}_k) = \mathcal{N}(\boldsymbol{s}_k; \boldsymbol{v}(\boldsymbol{s}_{k-1}, \boldsymbol{u}_k), \boldsymbol{Q}_k), \tag{2.1}$$

where $\boldsymbol{u}_k$ denotes the control variable, representing certain known local information at the UE side, $\boldsymbol{v}(\cdot)$ denotes the known transition function derived from local information, and $\boldsymbol{Q}_k$ represents the covariance of the process noise.

Landmarks

Two distinct types of unknown landmarks are considered: scattering points (SPs) and surfaces. An SP, representing a small object such as a street lamp or traffic sign, solely scatters signals. It is parameterized by its location $\boldsymbol{x}_{\mathrm{SP}} = [x_{\mathrm{SP},k}, y_{\mathrm{SP},k}, z_{\mathrm{SP},k}]^\top$, equivalent to the incidence point (IP) where the signal encounters the landmark.

On the other hand, a surface, corresponding to a larger object such as a wall or building facade, reflects (and possibly diffuses, depending on scenario assumptions) signals. It is parameterized by a fixed virtual anchor (VA) with a location denoted as $\boldsymbol{x}_{\mathrm{VA}} = [x_{\mathrm{VA},k}, y_{\mathrm{VA},k}, z_{\mathrm{VA},k}]^\top$. The VA is surface-specific, determined by the reflection of the BS with respect to the surface, given by [53]

$$\boldsymbol{x}_{\mathrm{VA}} = (\boldsymbol{I} - 2\boldsymbol{\nu}\boldsymbol{\nu}^\top)\boldsymbol{p}_{\mathrm{BS}} + 2\boldsymbol{\mu}^\top\boldsymbol{\nu}\boldsymbol{\nu}, \tag{2.2}$$

where $\boldsymbol{\nu}$ signifies the surface normal, and $\boldsymbol{\mu}$ represents an arbitrary point on the surface. Notably, a VA remains stationary even though the IP of the reflection path on the surface changes with the movement of the UE. Additionally, multiple IPs on the surfaces could exist from the reflection path and the diffuse multipath at each time step, assuming the surface can both reflect and diffuse signals.

2.2 Measurement model

During each time step, the BS transmits downlink orthogonal frequency-division multiplexing (OFDM) pilot signals to the UE. These signals can traverse the communication channel through the LoS path, where signals directly reach the UE, or through NLoS paths, where signals bounce off landmarks in the environment before reaching the UE, or a combination of both. At time step k, a channel estimator, as exemplified in [54–58], can be employed on the received pilot signals to obtain estimates of channel parameters, i.e., time-of-arrival (ToA), angle-of-arrival (AoA), and angle-of-departure (AoD) as measurements. While the gain may contain geometric information, it is significantly influenced by other factors such as surface material, weather, and temperature. Consequently, it is not utilized as part of the measurements in Part I.

Channel estimation is assumed to be outside the scope of this thesis, and the channel parameters are considered available, serving directly as measurements. In addition, only LoS and single-bounce paths are considered. At time step k, the channel estimator produces a list of measurements denoted as $\mathcal{Z}_k = \{\boldsymbol{z}_k^1, \ldots, \boldsymbol{z}_k^{I_k}\}$. It is important to acknowledge that the number of measurements I_k in general is not the same as the total number of ground-truth paths, since not all paths can be resolved. Some measurements may be clutter originating from noise peaks during channel estimation or transient objects, and certain landmarks might be misdetected. Furthermore, the DA problem remains unsolved, implying that the source of each measurement is unclear. For any $\boldsymbol{z}_k^i \in \mathcal{Z}_k$ originating from a landmark with an IP location $\boldsymbol{x}_{\mathrm{IP},k}^i$, the likelihood function is modeled by

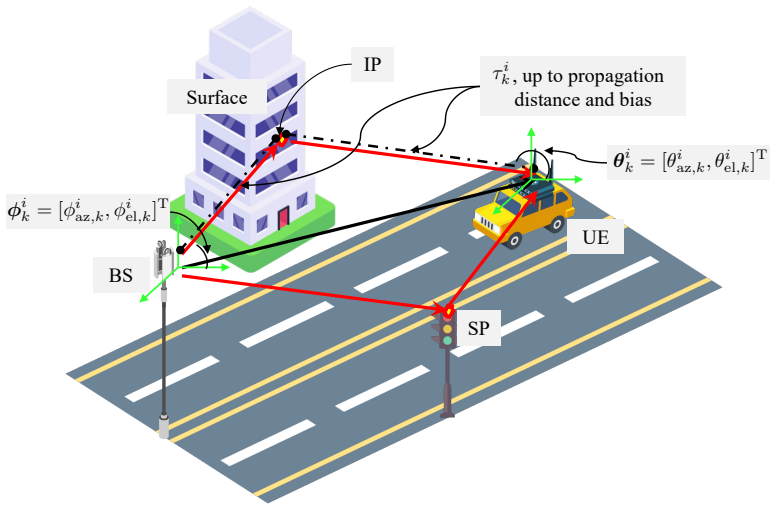

Figure 2.2: Illustrative demonstration of the nonlinear measurement function, which translates geometric information into channel parameters.

$$f(\boldsymbol{z}_k^i|\boldsymbol{x}_{\text{IP},k}^i, \boldsymbol{s}_k) = \mathcal{N}(\boldsymbol{z}_k^i; \boldsymbol{h}(\boldsymbol{x}_{\text{IP},k}^i, \boldsymbol{s}_k), \boldsymbol{R}_k^i), \tag{2.3}$$

where $\boldsymbol{h}(\boldsymbol{x}_{\text{IP},k}^i, \boldsymbol{s}_k) = [\tau_k^i, (\boldsymbol{\theta}_k^i)^\text{T}, (\boldsymbol{\phi}_k^i)^\text{T}]^\text{T}$ serves as the nonlinear measurement function, converting geometric information into channel parameters, and $\boldsymbol{R}_k^i$ represents the measurement covariance. Fig. 2.2 provides an illustrative representation of the $\boldsymbol{h}(\boldsymbol{x}_{\text{IP},k}^i, \boldsymbol{s}_k)$.

Within the measurement function $\boldsymbol{h}(\boldsymbol{x}_{\text{IP},k}^i, \boldsymbol{s}_k)$, the ToA τ_k^i is determined by the propagation distance and the clock bias b_k, expressed as

$$\tau_k^i = \begin{cases} \frac{\|\boldsymbol{p}_{\text{BS}} - \boldsymbol{p}_{\text{UE},k}\|}{c} + b_k & \text{LoS} \\ \frac{\|\boldsymbol{x}_{\text{IP},k}^i - \boldsymbol{p}_{\text{UE},k}\| + \|\boldsymbol{x}_{\text{IP},k}^i - \boldsymbol{p}_{\text{BS}}\|}{c} + b_k & \text{NLoS} \end{cases}, \tag{2.4}$$

with c denoting the speed of light.

The AoA $\boldsymbol{\theta}_k^i = [\theta_{\text{az},k}^i, \theta_{\text{el},k}^i]^\text{T}$, consisting of the azimuth and elevation angles, is determined by the arrival direction of the signal at the receiver $\boldsymbol{q}_{\text{AOA},k}^i$, and its components are given by

$$\theta_{\text{az},k}^i = \text{arctan2}([\boldsymbol{q}_{\text{AOA},k}^i]_2, [\boldsymbol{q}_{\text{AOA},k}^i]_1), \tag{2.5}$$
$$\theta_{\text{el},k}^i = \text{arcsin}([\boldsymbol{q}_{\text{AOA},k}^i]_3, \|\boldsymbol{q}_{\text{AOA},k}^i\|). \tag{2.6}$$

The arrival direction of the signal $\boldsymbol{q}_{\text{AOA},k}^i$ is considered in the local coordinate system of

the receiver, enabling its calculation through

$$\boldsymbol{q}^i_{\mathrm{AOA},k} = \begin{cases} \boldsymbol{R}_{\mathrm{UE},k}(\boldsymbol{p}_{\mathrm{BS}} - \boldsymbol{p}_{\mathrm{UE},k}) & \text{LoS} \\ \boldsymbol{R}_{\mathrm{UE},k}(\boldsymbol{x}^i_{\mathrm{IP},k} - \boldsymbol{p}_{\mathrm{UE},k}) & \text{NLoS,} \end{cases} \tag{2.7}$$

where $\boldsymbol{R}_{\mathrm{UE},k}$ is the rotation matrix from the reference coordinate system to the local coordinate system of the URA at the UE side and time step k, determined by $\boldsymbol{\psi}_{\mathrm{UE},k}$ as [52]

$$\boldsymbol{R}_{\mathrm{UE},k} = \tag{2.8}$$
$$\begin{bmatrix} \cos\gamma_{\mathrm{UE},k} & -\sin\gamma_{\mathrm{UE},k} & 0 \\ \sin\gamma_{\mathrm{UE},k} & \cos\gamma_{\mathrm{UE},k} & 0 \\ 0 & 0 & 1 \end{bmatrix} \begin{bmatrix} \cos\beta_{\mathrm{UE},k} & 0 & \sin\beta_{\mathrm{UE},k} \\ 0 & 1 & 0 \\ -\sin\beta_{\mathrm{UE},k} & 0 & \cos\beta_{\mathrm{UE},k} \end{bmatrix} \begin{bmatrix} 1 & 0 & 0 \\ 0 & \cos\alpha_{\mathrm{UE},k} & -\sin\alpha_{\mathrm{UE},k} \\ 0 & \sin\alpha_{\mathrm{UE},k} & \cos\alpha_{\mathrm{UE},k} \end{bmatrix},$$

and $\boldsymbol{R}^{\mathsf{T}}_{\mathrm{UE},k}$ denotes the rotation matrix from the local coordinate system of the UE to the reference coordinate system.

Similarly, the AoD $\boldsymbol{\phi}^i_k = [\phi^i_{\mathrm{az},k}, \phi^i_{\mathrm{el},k}]^{\mathsf{T}}$, consisting of the azimuth and elevation angles, is determined by the departure direction of the signal at the transmitter $\boldsymbol{q}^i_{\mathrm{AOD},k}$, and its components are given by

$$\phi^i_{\mathrm{az},k} = \arctan2([\boldsymbol{q}^i_{\mathrm{AOD},k}]_2, [\boldsymbol{q}^i_{\mathrm{AOD},k}]_1), \tag{2.9}$$
$$\phi^i_{\mathrm{el},k} = \arcsin([\boldsymbol{q}^i_{\mathrm{AOD},k}]_3, \|\boldsymbol{q}^i_{\mathrm{AOD},k}\|). \tag{2.10}$$

The departure direction of the signal $\boldsymbol{q}^i_{\mathrm{AOD},k}$ is considered in the local coordinate system of the transmitter, given by

$$\boldsymbol{q}^i_{\mathrm{AOD},k} = \begin{cases} \boldsymbol{R}_{\mathrm{BS}}(\boldsymbol{p}_{\mathrm{UE},k} - \boldsymbol{p}_{\mathrm{BS}}) & \text{LoS} \\ \boldsymbol{R}_{\mathrm{BS}}(\boldsymbol{x}^i_{\mathrm{IP},k} - \boldsymbol{p}_{\mathrm{BS}}) & \text{NLoS,} \end{cases} \tag{2.11}$$

where $\boldsymbol{R}_{\mathrm{BS}}$ is the rotation matrix from the reference coordinate system to the local coordinate system of the URA at the BS side. This matrix is determined by $\boldsymbol{\psi}_{\mathrm{BS}}$ as

$$\boldsymbol{R}_{\mathrm{BS}} = \begin{bmatrix} \cos\gamma_{\mathrm{BS}} & -\sin\gamma_{\mathrm{BS}} & 0 \\ \sin\gamma_{\mathrm{BS}} & \cos\gamma_{\mathrm{BS}} & 0 \\ 0 & 0 & 1 \end{bmatrix} \begin{bmatrix} \cos\beta_{\mathrm{BS}} & 0 & \sin\beta_{\mathrm{BS}} \\ 0 & 1 & 0 \\ -\sin\beta_{\mathrm{BS}} & 0 & \cos\beta_{\mathrm{BS}} \end{bmatrix} \begin{bmatrix} 1 & 0 & 0 \\ 0 & \cos\alpha_{\mathrm{BS}} & -\sin\alpha_{\mathrm{BS}} \\ 0 & \sin\alpha_{\mathrm{BS}} & \cos\alpha_{\mathrm{BS}} \end{bmatrix}, \tag{2.12}$$

and $\boldsymbol{R}^{\mathsf{T}}_{\mathrm{BS}}$ is the rotation matrix from the local coordinate system of the BS to the reference coordinate system.

CHAPTER 3

Single snapshot radio positioning and mapping

The radio positioning and mapping problem can be addressed on a snapshot-by-snapshot basis, without relying on memory from previous time steps. This chapter starts with introducing the challenge of single snapshot radio positioning and mapping, then examining classical positioning methods from the literature. Finally, strategies are explored for effectively addressing the problem, particularly in the context of 5G mmWave scenarios with a single BS.

3.1 Problem statement

The single snapshot radio positioning and mapping problem refers to an intricate task of estimating the state of the UE and mapping the surrounding environment from the signals received at the UE during a singular time step [33], as illustrated in Fig. 3.1. In this challenging scenario, the primary objective is to unravel the precise UE state while concurrently generating a comprehensive representation of the landmarks in the surrounding physical space. It is noteworthy that UE state and landmark states can comprise diverse components, and the specific composition may vary across different problems [7, 59–61]. The target UE state usually encompasses, at a minimum, the UE position and may extend to include additional parameters such as UE orientation, clock bias between the BS and the UE, and other relevant properties. Similarly, the target landmark state usually comprises, at a minimum, location information and may encompass additional characteristics like landmark types, size, or other pertinent attributes.

In this context, the term "*snapshot*" denotes a discrete moment in time when the UE

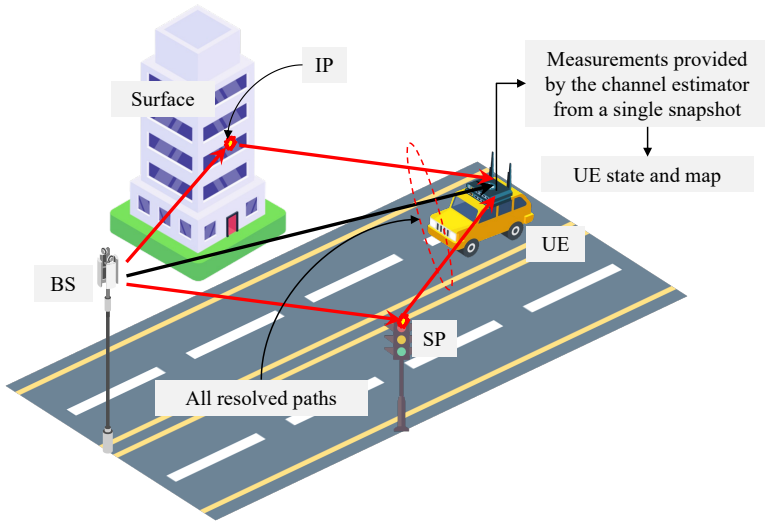

Figure 3.1: Illustrative demonstration of the single snapshot positioning and mapping problem, where all resolved measurements from a single snapshot are employed to estimate the UE state and the surrounding environment.

receives radio signals, which are the downlink signals sent from the BS that pass through the complex environment and then reach the UE. These received signals offer a brief glimpse into the spatial and signal characteristics at that specific instant. We assume that the channel estimator is already implemented on the single snapshot received signals, which directly provides the channel parameter estimates, i.e., gains, delays, and angles, termed as the measurements in this thesis. Instead of working with the raw received signals, we directly employ these measurements in the subsequent discussions. Then, the challenge lies in how to utilize these measurements extrapolated from single snapshot received signals to determine the UE state and construct a map of the surrounding environment.

This problem domain is particularly relevant in applications such as dense urban scenarios and indoor localization, where GNSS may be unreliable [21]. The ability to robustly estimate the state of the UE and map the environment based on a solitary snapshot holds significance in diverse fields, including Internet of Things (IoT) devices [39], personal radar [62], smart homes [63], and location-based services [64, 65].

3.2 Classical positioning methods

Radio positioning is a well-established field that has garnered attention over many years. The fundamental concept revolves around extracting geometric information from radio

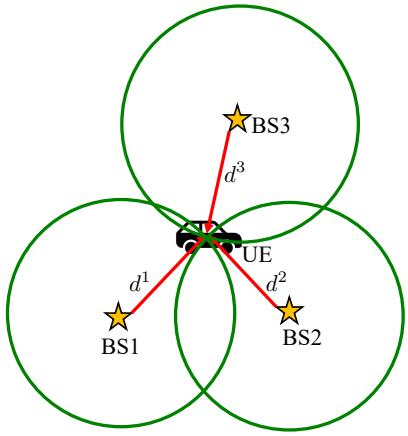

Figure 3.2: An example of ToA-based positioning method in a 2D scenario involving three BSs.

signals to enable positioning. This section provides an overview of classical positioning methods in the literature.

3.2.1 Time-based positioning

Some studies leverage ToA measurements from multiple LoS paths between various BSs and the UE for positioning purposes [5, 66]. ToA represents the measured time at which a signal arrives at a receiver. The relationship between the distance d^i from the i-th BS to the UE and the ToA τ^i of the corresponding LoS path is defined in (2.4), yielding

$$d^i = (\tau^i - b^i)c, \tag{3.1}$$

where b^i denotes the clock bias of the UE with respect to the i-th BS. Once distances from the UE to multiple BSs are obtained from LoS paths, the UE position can be estimated by satisfying geometric constraints, i.e., the distances to the BSs. Taking a 2D scenario as an example, illustrated in Fig. 3.2, we can draw a circle centered at each BS with a radius equal to the known distance between the UE and that specific BS. With the distances from the UE to three different BSs, three circles can be drawn. The intersection point of these circles corresponds to the UE position [20].

However, this method presents certain challenges. First of all, all BS positions should be known to the UE, and the LoS paths should be guaranteed. Notably, the accuracy of distance estimation is significantly influenced by clock bias, enlarged by the speed of light c in (3.1). To mitigate this, synchronization between each BS and the UE becomes imperative. Alternatively, identifying and compensating for clock biases at the UE side is necessary. Another approach involves employing a round-trip-time (RTT) protocol, utilizing round-trip (or two-way) ToA measurements [67–69]. An additional

strategy to address clock bias issues is the use of TDoA measurements, which is the difference between two ToA measurements [70, 71]. It is essential to note that for TDoA measurements, synchronization among all BSs is essential.

Furthermore, the accuracy of ToA estimates is influenced by factors such as available bandwidth and noise, impacting overall positioning performance [72]. Moreover, this methodology encounters significant challenges posed by multipath effects [73, 74]. Multipath introduces complications such as inter-path interference and may lead to the failure of the channel estimator in identifying the LoS path. Consequently, this can result in substantial errors in ToA estimates associated with the LoS path.

3.2.2 Angle-based positioning

Angular measurements, specifically AoA and AoD, which respectively denote the direction of signal arrival at the UE and departure from the BS, offer valuable insights for UE positioning [5, 66]. Unlike methods reliant on distance to a specific BS, angular measurements provide directional information toward the BS. By determining the AoA or the AoD of the LoS path from the i-th BS, and knowing the BS position, a line can be defined in the corresponding direction

$$\boldsymbol{p}^i = \boldsymbol{p}^i_{\mathrm{BS}} + m\boldsymbol{q}^i, \tag{3.2}$$

where $\boldsymbol{p}^i$ describes any point on the line, $\boldsymbol{p}^i_{\mathrm{BS}}$ denotes a specific point on the line which is the position of the i-th BS, $\boldsymbol{q}^i$ denotes the direction of the line determined by the AoA or the AoD, and m is a parameter varying across real numbers. This line inherently contains the UE position. By finding the intersection point of multiple observed lines (corresponding to different BSs), the UE position can be accurately determined [20]. Fig. 3.3 provides an illustrative example of an AoD-based positioning method in a 2D scenario with three BSs. In this scenario, the UE estimates the AoDs of three LoS paths from different BSs, allowing the determination of lines that intersect at the UE position.

However, achieving angular resolution in this method necessitates the use of multiple antennas. The accuracy of angle estimates is intricately tied to both the angular resolution and the presence of noise, introducing consequential impacts on overall positioning performance [75]. Similar to time-based positioning techniques, this approach encounters substantial challenges posed by multipath effects [5]. The prevalence of inter-path interference, coupled with potential ambiguities in distinguishing the LoS path from other NLoS paths, results in notable errors in angle estimates. These errors significantly undermine the effectiveness of the positioning system. Additionally, accurate knowledge of UE or BS orientations is crucial when employing AoA or AoD measurements. The AoA and AoD values are inherently dependent on the orientations of the UE and BS, respectively, as articulated in (2.7) and (2.11). It is worth noting that this method exhibits diminished performance over large distances, as even a small angular error can propagate into a substantial mismatch in such scenarios.

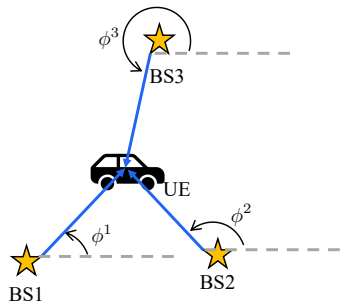

Figure 3.3: An example of AoD-based positioning method in a 2D scenario involving three BSs.

3.3 Single BS positioning and mapping

The classical positioning methods discussed in Section (3.2) rely on the availability of multiple BSs, and their performances are subject to limitations in geometric measurement resolution imposed by bandwidth and antenna size constraints. These methods are also susceptible to severe multipath effects. Moreover, these approaches exclusively focus on estimating UE position, leaving aspects such as UE orientation and clock bias estimation, as well as the mapping problem, unresolved due to insufficient information from the measurements.

The advent of 5G (and potentially the future 6G) systems presents new opportunities and possibilities for positioning [21]. In 5G, higher carrier frequencies, such as above 24 GHz, are achievable [2]. At these frequencies, limited scattering leads to sparse communication channels. The increased carrier frequency allows for a larger bandwidth, resulting in improved time-delay resolution and enhanced distance estimation accuracy [5]. Additionally, larger antenna arrays with more elements at both UE and BS sides enable higher resolution in AoA and AoD [4]. With these advantages, paths become more resolvable, providing a greater number of measurements and additional dimensions with significantly enhanced accuracy for each resolved path [6]. For instance, accurate estimates for 5D measurements (ToA, AoA in both azimuth and elevation, AoD in both azimuth and elevation) become feasible, as opposed to rough estimates for ToA alone. Furthermore, the improved resolution allows for the resolution of multipath, traditionally regarded as a disturbance, offering valuable information about both the map and the UE state. This abundance of information makes both positioning (including position, orientation and clock bias), and mapping viable, even with a single BS, as there is now sufficient information to address both problems [33].

While multiple BSs can provide additional measurements, resulting in improved positioning and mapping performance, this section specifically focuses on single BS positioning and mapping due to its inherent significance and feasibility.

3.3.1 Requirements

To address the single BS positioning and mapping problem, certain prerequisites must be fulfilled. The subsequent discussion outlines the essential requirements for solving the single BS positioning and mapping problem.

BS state

For the successful realization of single BS positioning and mapping, precise knowledge of the BS position and orientation is essential to establish an accurate global reference coordinate. It is not strictly required in theory to have explicit knowledge of the BS for problem resolution, as long as a global reference is provided, such as by a known reflector in the environment. Knowing the BS is generally the most reasonable and practical requirement. Typically, BS position and orientation are available with high accuracy, given the fixed nature of BS installations, allowing for precise measurements using external equipment. Despite the theoretical potential to survey BS state with arbitrary accuracy, practical limitations introduce inevitable errors.

Additionally, considering that BSs are primarily designed for communication rather than accurate positioning, only coarse BS state information may be available [38]. This could involve manual measurement errors or slight changes in the deployed position and orientation over extended periods. As measurements depend on the BS position and orientation, errors in these parameters can lead to significant inaccuracies in positioning and mapping, especially over long distances. Therefore, in cases where explicit site surveying has not been conducted, an additional calibration process for BS position and orientation becomes necessary.

Enough useful geometric parameters

The positioning and mapping problem involves estimating the UE state and the map of the surrounding environment based on all resolved measurements, including ToAs, AoAs, and AoDs [33]. For each LoS path, we can obtain up to 5 useful geometric parameters when the UE orientation is unknown and up to 3 when the UE orientation is known. This is due to the fact that AoA and AoD contain the same information when both the BS orientation and the UE orientation are known. For each NLoS path, we can extract up to 5 useful geometric parameters when the IP is unknown and up to 3 when the IP is known. This is attributed to the fact that AoD can be determined once both the BS and the corresponding IP are known, rendering it uninformative for positioning and mapping.

A summary of the number of useful geometric parameters for a 5D measurement in different cases within a MIMO scenario with planar antenna arrays at both BS and UE sides is provided in Table 3.1. In a 3D scenario, the unknown parameters typically include a 3D UE position, a 3D UE orientation, a 1D clock bias, and a 3D position for the IP of each NLoS path. A summary of the number of unknowns for different types of problems in a 3D scenario is presented in Table 3.2. Assuming there are N_x unknowns and N_y useful geometric parameters in total, the necessary condition for addressing the

	Number of useful geometric parameters
LoS, unknown UE orientation	5
LoS, known UE orientation	3
NLoS, unknown IP	5
NLoS, known IP	3

Table 3.1: Summary of number of useful geometric parameters for a 5D measurement in different cases within a MIMO scenario with planar antenna arrays at both BS and UE sides.

	Number of unknowns N_x
UE position	3
UE position + clock bias	4
UE position + UE orientation	6
UE position + UE orientation + clock bias	7
UE position + UE orientation + clock bias + mapping	$7 + 3L$

Table 3.2: Summary of number of unknowns for different types of problems in a 3D scenario, where L denotes the number of unknown IPs.

positioning and mapping problem is

$$N_x \leq N_y. \tag{3.3}$$

3.3.2 LoS-only positioning

If only the LoS between the BS and the UE is available, it is possible to estimate the UE position. However, synchronizing the UE with the BS or estimating the UE orientation is not feasible without additional information. The LoS path can provide at most 5 useful geometric parameters when the UE orientation is unknown, which is insufficient to estimate both the UE position and orientation, involving 6 unknowns. If the AoA is not utilized, the LoS path provides 3 useful geometric parameters, allowing for the estimation of 3 unknown variables, and thus, the UE position can be estimated. When the clock bias between the BS and the UE is known or eliminated by the RTT protocol, the UE position $\boldsymbol{p}_{\mathrm{UE}}$ has a closed-form solution [26, 76]

$$\boldsymbol{p}_{\mathrm{UE}} = \boldsymbol{p}_{\mathrm{BS}} + d_{\mathrm{LoS}}\boldsymbol{u}_{\mathrm{LoS}}, \tag{3.4}$$

where $d_{\mathrm{LoS}} = (\tau_{\mathrm{LoS}} - b)c$ denotes the propagation distance of the LoS path, and $\boldsymbol{u}_{\mathrm{LoS}}$ represents the unit vector describing the direction from the BS to the UE, determined

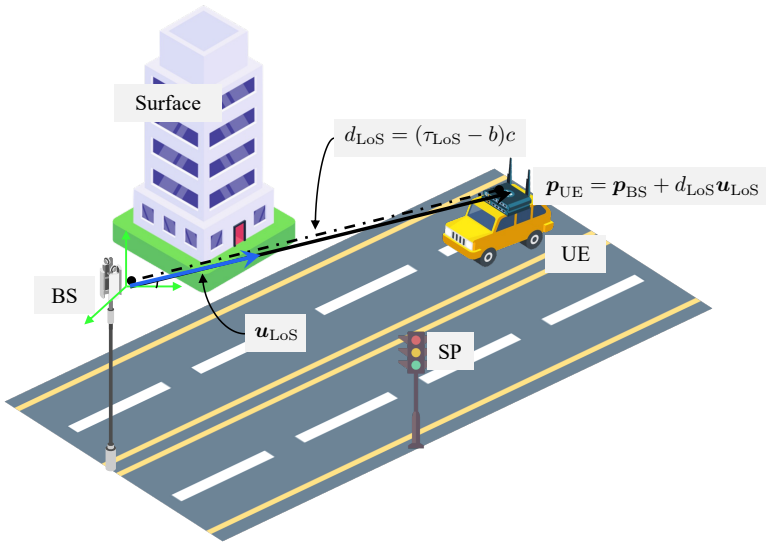

Figure 3.4: Illustrative demonstration of LoS-only positioning, where the UE is positioned at a distance d_{LoS} from the BS along the direction of $\boldsymbol{u}_{\mathrm{LoS}}$. NLoS path are omitted to emphasize the LoS path, though they do exist.

by the AoD as

$$\boldsymbol{u}_{\mathrm{LoS}} = \boldsymbol{R}_{\mathrm{BS}}^{\mathsf{T}} \begin{bmatrix} \cos\left(\phi_{\mathrm{az,LoS}}\right)\cos\left(\phi_{\mathrm{el,LoS}}\right) \\ \sin\left(\phi_{\mathrm{az,LoS}}\right)\cos\left(\phi_{\mathrm{el,LoS}}\right) \\ \sin\left(\phi_{\mathrm{el,LoS}}\right) \end{bmatrix}. \tag{3.5}$$

The fundamental concept behind (3.4) is that the UE is positioned at a distance d_{LoS} from the BS along the direction of $\boldsymbol{u}_{\mathrm{LoS}}$, as illustrated in Fig. 3.4. Additionally, if the UE orientation is known, $\boldsymbol{u}_{\mathrm{LoS}}$ can be also determined by AoA, expressed as

$$\boldsymbol{u}_{\mathrm{LoS}} = -\boldsymbol{R}_{\mathrm{UE}}^{\mathsf{T}} \begin{bmatrix} \cos\left(\theta_{\mathrm{az,LoS}}\right)\cos\left(\theta_{\mathrm{el,LoS}}\right) \\ \sin\left(\theta_{\mathrm{az,LoS}}\right)\cos\left(\theta_{\mathrm{el,LoS}}\right) \\ \sin\left(\theta_{\mathrm{el,LoS}}\right) \end{bmatrix}. \tag{3.6}$$

However, this method is not commonly employed because the UE orientation is usually unknown. In an ideal scenario where both the clock bias and UE orientation are provided, all 5 geometric parameters can be utilized to estimate the UE position. Taking both AoA and AoD into consideration to determine $\boldsymbol{u}_{\mathrm{LoS}}$, the estimated UE position $\boldsymbol{p}_{\mathrm{UE},k}$ can be obtained through a maximum likelihood (ML) estimator

$$\hat{\boldsymbol{p}}_{\mathrm{UE}} = \underset{\boldsymbol{p}_{\mathrm{UE}}}{\arg\min} \left(\left(\boldsymbol{h}(\boldsymbol{p}_{\mathrm{UE}}) - \boldsymbol{z}_{\mathrm{LoS}}\right)^{\mathsf{T}} \left(\boldsymbol{R}_{\mathrm{LoS}}\right)^{-1} \left(\boldsymbol{h}(\boldsymbol{p}_{\mathrm{UE}}) - \boldsymbol{z}_{\mathrm{LoS}}\right) \right), \tag{3.7}$$

	Minimum number of NLoS paths
Map-assisted, LOS+NLOS	1
Map-assisted, NLOS	3
No map, LOS+NLOS	1
No map, NLOS	4

Table 3.3: Summary of the minimum number of NLoS paths needed for full UE positioning in different scenarios.

where $\boldsymbol{h}(\boldsymbol{p}_{\mathrm{UE}})$ is the measurement function using the UE position to generate the 5D measurement of the LoS path. Please note (3.4) is a special case of (3.7), where only ToA, and AoD are used. This method works well in an ideal case, however, it is sensitive to the measurement quality, as only one group of measurements is used. The real measurement contains errors, which results in large positioning errors, especially in a long distance. In addition, the clock bias needs to be known or eliminated for this method, which is usually not easy to achieve.

3.3.3 Multipath-assisted positioning

If multipath is considered as a disturbance and only the LoS path is utilized, limited position information can be obtained, restricting the capability to solve the positioning problem. However, the resolved multipath components also contain geometric information about the UE state, which can be beneficial for the positioning problem [33]. In the context of the complete positioning problem, which involves estimating the UE position and UE orientation while synchronizing it with the BS, the LoS path provides 5 useful geometric parameters. Additionally, each NLoS path can offer 3 useful geometric parameters if the corresponding IP is known and 5 useful geometric parameters if the IP is unknown. However, the latter introduces three unknowns to the problem.

For the map-assisted positioning problem, where the IP of each NLoS is known, the full positioning problem is solvable if both the LoS path and another additional NLoS path are available. In this case, there are 8 useful geometric parameters versus 7 unknowns. The problem remains solvable even if the LoS path is obstructed by obstacles. At least three resolved NLoS paths are required for the problem to be solvable, resulting in 9 useful geometric parameters versus 7 unknowns.

The problem can also be solved without relying on map assistance. If the LoS path is available, at least one more NLoS path should be resolved, resulting in 10 useful geometric parameters versus 10 unknowns. In scenarios where the LoS path is blocked, a minimum of 4 NLoS paths is needed, leading to 20 useful geometric parameters versus 19 unknowns. The minimum numbers of NLoS paths needed for full UE positioning in different cases are summarized in Table 3.3. Once the requirements are fulfilled, the full positioning problem can be approached using a ML estimator, aiming to identify

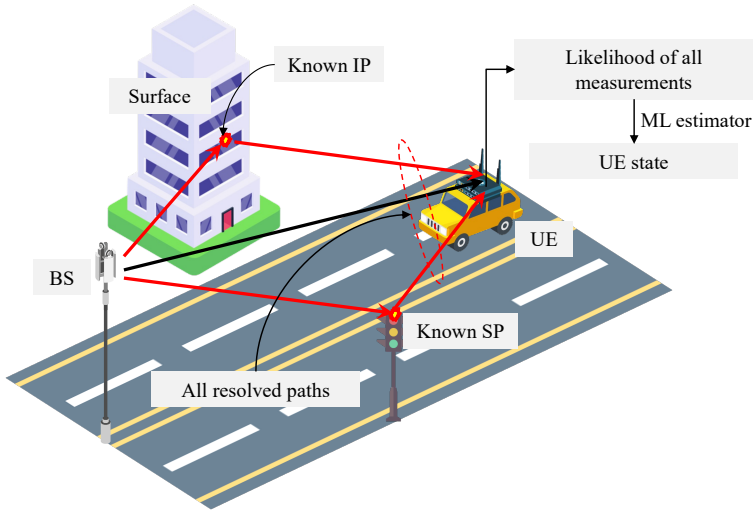

Figure 3.5: Illustrative demonstration of map-assisted positioning, where the IPs of each paths are known, and all resolved paths from a single snapshot are employed to estimate the UE state using a ML estimator.

the UE state that maximizes the likelihood of all received measurements, as exemplified in [61]. The performance of this method enhances with an increased number of resolved paths, as it provides more information for accurate estimation. Fig. 3.5 presents an illustrative showcase of map-assisted positioning. The crucial distinction between map-assisted positioning and positioning without map assistance lies in the availability of IP for each path.

3.3.4 From positioning to mapping

As discussed in Section 3.3.3, multipath encompasses crucial geometric information about both the UE state and the surrounding map, facilitating both UE positioning and environmental mapping [33]. Referring to Table 3.3, the positioning and mapping problem can be resolved with a minimum of one additional NLoS path if the LoS path is available, and at least 4 NLoS paths if the LoS path is unavailable. Similar to the approach for solving the positioning problem using multipath, this combined positioning and mapping problem can also be formulated as a ML problem. In this scenario, the objective is to identify the UE state and all IP positions that maximize the likelihood of all received measurements, as exemplified in [60].

After obtaining all the IPs positions, post-processing steps can be applied based on specific requirements. One possible post-processing task involves estimating surfaces from these IPs. The underlying concept is that each IP represents the point where the

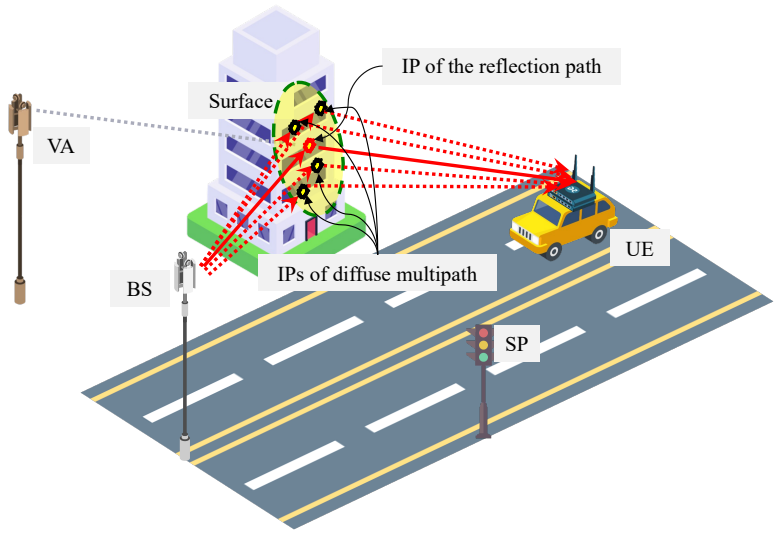

Figure 3.6: Illustrative presentation of an example featuring a reflection path and 4 diffuse multipath originating from a surface. The reflection path is depicted by a red solid line, while the diffuse multipath are represented by red dashed lines. The IP of the reflection path is determined by the VA, the UE and the surface, whereas the IPs of all diffuse multipath are randomly distributed on the surface. Notably, all IPs are confined to the surface. Paths from other sources are excluded to highlight the paths originating from the surface, even though additional paths exist.

signal interacts with a surface, and IPs of paths reflected or diffused from the same source should lie on the same surface, as illustrated in Fig. 3.6. Thus, the goal is to identify surfaces that best fit all estimated IPs associated with paths originating from the same surface.

However, at this stage, the source of each path is still unknown, except for the LoS path, which is usually assumed to be the strongest and shortest path. Therefore, direct estimation of surfaces from IPs is not feasible. To address this, it is necessary to cluster IPs of paths from the same source, leveraging the geometric proximity of IPs within the same cluster. An effective approach for this clustering task is the use of algorithms like density-based spatial clustering of applications with noise (DBSCAN) [77]. The DBSCAN algorithm categorizes points into clusters and identifies potential outlier points based on density-reachability. Each point cluster corresponds to a surface, and the surface associated with each cluster is determined by finding the best fit for all points within the cluster, minimizing the overall distances to the surface.

3.3.5 Discussions

The solution to the single BS positioning and mapping problems lies in addressing the ML problems discussed in Section 3.3.2, Section 3.3.3 and Section 3.3.4. Various studies employ different optimization methods, simplifications, assumptions, and utilized measurements. While considerable theoretical work has been undertaken, only a limited number of studies have conducted real-world experiments and tests, particularly involving a commercial BS. [Paper C] fills this gap by presenting a distinctive real-world demonstration of single BS 5G mmWave positioning and mapping. Moreover, it is common for a large surface to both reflect and diffuse signals. However, the consideration of multipath measurements from the same source has been relatively overlooked or simplified in existing works. In [Paper A], we introduce a method to utilize all multipath measurements originating from the same landmark.

CHAPTER 4

Single BS radio simultaneous localization and mapping

The positioning and mapping problem, discussed in Section 3.3, can be addressed through singular snapshot measurements employing only a single BS. Over time, this single BS positioning and mapping problem can be extended to incorporate UE tracking, transforming it into a SLAM problem known as radio SLAM. This chapter outlines the problem statement of radio SLAM and provides an overview of various SLAM frameworks applicable to the radio SLAM problem.

4.1 Problem statement

The SLAM problem generally involves estimating the sensor state over time, constructing a map of the surrounding environment, and assessing associated uncertainties [40,41]. In this context, the term "*over time*" refers to a continuous time span rather than a discrete moment, emphasizing the need to consider connections between different snapshots. The primary objective of the probabilistic SLAM problem is typically to determine or approximate the joint posterior density of the sensor trajectory and the map, denoted as $f(\boldsymbol{s}_{1:k}, \mathcal{X} | \mathcal{Z}_{1:k}, \boldsymbol{u}_{1:k}, \boldsymbol{s}_0)$, given the initial sensor state $\boldsymbol{s}_0$, measurements $\mathcal{Z}_{1:k}$ and controls $\boldsymbol{u}_{1:k}$ up to and including time step k.

The radio SLAM problem, specifically utilizing radio signals [9, 10], involves the UE serves as the sensor, possessing an unknown time-varying state, while the static objects in the environment act as landmarks with unknown states and cardinality, collectively forming the map. Similar to the single snapshot positioning and mapping problem discussed in Chapter 3, the UE state encompasses not only the UE position but potentially

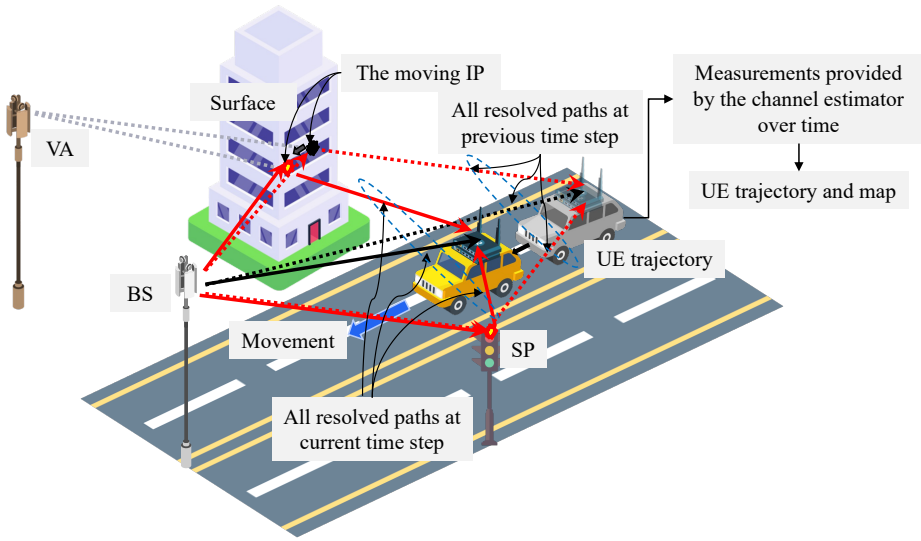

Figure 4.1: Illustrative demonstration of the radio SLAM problem, where resolved measurements over time are leveraged to estimate both the UE trajectory and the surrounding environment. Paths successfully resolved in the previous time step are depicted by dashed lines, while newly resolved paths in the current time step are represented by solid lines. The IP of the reflection path on the surface moves with the movement of the UE, whereas the VA of the surface remains static.

its orientation, clock bias with the BS, or other states varying across different scenarios. The landmark state usually includes only the position, but it may also encompass the landmark type, size, or other characteristics, depending on the specific problem. As in Chapter 3, we directly utilize the channel parameter estimates as measurements, assuming that the channel estimator has been implemented on the received signals. Fig. 4.1 provides an illustrative representation of the radio SLAM problem.

The radio SLAM problem is inherently challenging due to several factors [78]:

- Unknown number of landmarks: The map being unknown implies that the number of landmarks in the field-of-view (FoV) is primarily unknown to the UE.
- Clutter measurements: Channel estimation errors or noise peaks can result in numerous clutter measurements, potentially leading to false alarms.
- Imperfect detection: Landmarks in the FoV might go undetected due to imperfect detection performance at the UE side.
- Unknown DA: The UE lacks knowledge about the source of each measurement, introducing an inherent DA problem. This challenge involves associating measure-

ments with their sources, which could be previously detected landmarks, undetected landmarks, or measurements classified as clutter.

Desirable solutions for radio SLAM should address all these challenges effectively while maintaining reasonable signal processing complexity.

4.2 Methods for radio SLAM

This section provides an overview of various SLAM frameworks applicable to solving the radio SLAM problem. These encompass conventional SLAM solutions, GraphSLAM, BP-SLAM, and RFS-SLAM.

4.2.1 Conventional solutions

One of the pivotal characteristics of the SLAM problem is the conditional independence among landmarks when the map is conditioned on the UE trajectory. Exploiting this feature, it is natural to employ solutions such as Rao-Blackwellized particle filter (RBPF), exemplified by the well-known FastSLAM algorithm [79]. In FastSLAM, the SLAM posterior is factorized into a product of conditional landmark posterior on the UE trajectory and a UE trajectory posterior. FastSLAM involves utilizing a list of weighted particles to represent the UE trajectory posterior, with each particle having a conditioned map. The SLAM posterior is then propagated through these particles and conditional maps. However, the computational complexity of this method is high, requiring a substantial number of particles to achieve satisfactory performance. An alternative, low-complexity approach to SLAM involves approximating the joint posterior density as a Gaussian distribution. Techniques such as the extended Kalman filter (EKF) [80, Ch. 7.2] are then employed for posterior estimation, leading to the well-established extended Kalman (EK)-SLAM algorithm [81]. In EK-SLAM, the SLAM posterior is approximated through linearization, achieved using the first-order Taylor series. While this approach generally exhibits low complexity and performs well in practice, its efficacy diminishes when dealing with highly nonlinear measurement models. Importantly, classical SLAM methods, including FastSLAM and EK-SLAM, necessitate solving the DA problem in advance. The algorithm approximates the posterior by conditioning it on the provided DA without accounting for any DA uncertainty. Consequently, these methods are sensitive to DA uncertainty [82].

4.2.2 GraphSLAM

In the realm of GraphSLAM, the DA problem is commonly tackled through the SLAM front-end approach [82]. Once the DA is resolved, GraphSLAM algorithms proceed to compute the joint posterior density of the UE trajectory and landmarks by transforming this density into a graphical network [83]. In this graphical network, nodes represent UE states at different times or landmarks, while edges denote the constraints between two

UE states or between a landmark state and a UE state. These constraints encompass probability distributions over relative transformations, derived from either the motion model of the UE or the measurement model of the UE and landmarks [84]. Once the graph is established, the SLAM problem transforms into determining the most probable configuration of these nodes to maximize the posterior, where standard optimization techniques [85, 86] can be employed. It is noteworthy that GraphSLAM operates differently from certain other SLAM methods like EK-SLAM and FastSLAM, which operate online. GraphSLAM opts for batch estimation, where measurements are processed in batches. This approach, considering all measurements and applying optimization techniques across the entire graph, yields more robust and accurate estimates, if conditioned on a reliable DA. However, it is crucial to emphasize that achieving a good DA is essential for the effectiveness of GraphSLAM.

4.2.3 BP-SLAM

Efficient resolution of the SLAM problem can be achieved by computing the marginal posterior densities of the landmarks and the UE state. An effective approach to approximating these marginal posterior densities in SLAM is through BP, specifically utilizing the sum-product algorithm [87]. This method is commonly referred to as BP-SLAM [9, 88–90]. BP-SLAM algorithms offer a unified framework for solving SLAM problems without the necessity of resolving the DA beforehand. In these algorithms, auxiliary variables are introduced to represent DAs, and BP is employed on the factor graph representation of the joint distribution of UE states, landmarks, and DA variables. BP-SLAM is a powerful approach due to its generality in handling complex scenarios. However, it has limitations. Notably, the correlation between the UE state and the map cannot be explicitly tracked in BP-SLAM due to the application of marginalization during the BP process. Additionally, ad-hoc modifications are often required to address challenges related to appearing and disappearing landmarks.

4.2.4 RFS-SLAM

The SLAM problem can be effectively addressed using the RFS theory. An RFS is a random variable whose potential outcomes are sets with a finite number of unique elements. Unlike random vectors, where both the number and order of elements are predetermined, RFSs have a random number of elements, and are agnostic to the order of elements, allowing for easy addition or removal of elements [49,91]. These characteristics make RFSs particularly appealing for modeling unknown landmarks and received measurements in the SLAM problem. The inherent ability of RFSs to capture uncertainty in both the number of landmarks and their states, as well as the DA uncertainty, renders them suitable for SLAM applications. Various RFS-SLAM methods employ different types of RFSs to model landmarks, such as the labeled multi-Bernoulli (LMB) RFS [92, 93], the δ-generalized labeled multi-Bernoulli (δ-GLMB) RFS [94, 95], the Poisson point pro-

cess (PPP) RFS [78, 91, 96], and the PMBM RFS [97–101]. Each choice results in a joint posterior with distinct RFS characteristics. Similar to the aforementioned SLAM algorithms, RFS-SLAM algorithms aim to obtain the joint posterior of the UE trajectory and the map over time. The key difference lies in modeling the map and measurements as RFSs and leveraging RFS-based statistics. Details on the RFS theory and the application of RFS-SLAM in a radio scenario will be elaborated upon in subsequent chapters.

CHAPTER 5

Random finite sets – a brief introduction

RFSs refer to random sets with a finite number of elements, commonly employed in multi-object tracking (MOT) and SLAM problems. This chapter delves into the fundamental concepts of RFSs, their statistical properties, key RFSs, and prevalent metrics for assessing the disparity between two RFSs. For more in-depth exploration, readers are encouraged to consult [49, 102].

5.1 Definition

An RFS is a random variable whose possible outcomes are sets with a finite number of unique elements. To be exact, in an RFS, $\mathcal{X} = \{\boldsymbol{x}^1, \boldsymbol{x}^2, \ldots, \boldsymbol{x}^n\}$, both the number of elements and the elements themselves are random [49, Section 2.3]. The elements within an RFS belong to the same space $\mathbb{D}$, which is typically an Euclidean space with a specific dimension. It is important to note that the space $\mathbb{D}$ may vary for different RFSs. RFSs adhere to the properties of sets:

- Two sets are considered equal if they contain exactly the same elements.
- Sets are order-invariant, e.g., $\{1, 2\} = \{2, 1\}$.
- Sets do not include repeated elements, e.g., $\{1, 1, 2\}$ is not a valid set.
- An empty set is denoted as $\varnothing$ and contains no elements.
- Two sets are disjoint if their intersection is empty, i.e., $\mathcal{X} \cap \mathcal{Y} = \varnothing$.

5.2 Statistics

This section delves into fundamental concepts and statistical principles integral to the theory of RFSs.

Multi-object density

The distribution of an RFS $\mathcal{X}$ is characterized by its multi-object probability density function (PDF), denoted as $f(\mathcal{X})$, also referred to as the multi-object density. This non-negative function sums to one and encapsulates the distribution over the cardinality as well as the distribution over elements of the set (given the cardinality) [49, Section 3.2.4, 4.2.2].

Set integral

The set integral of a multi-object density is defined as [49, Section 3.3]

$$\int f(\mathcal{X})\delta\mathcal{X} = \sum_{i=0}^{\infty} \frac{1}{i!} \int f(\{\boldsymbol{x}^1, \boldsymbol{x}^2, \ldots, \boldsymbol{x}^i\}) \mathrm{d}\boldsymbol{x}^1 \ldots \mathrm{d}\boldsymbol{x}^i. \tag{5.1}$$

The set integral encompasses summation across all potential cardinalities and integration over all possible values of elements in the set for each cardinality.

Convolution formula

If $\mathcal{X}^1, \ldots, \mathcal{X}^n$ are independent RFSs, with $f^1(\mathcal{X}^1), \ldots, f^n(\mathcal{X}^n)$ as their multi-object densities, then the union of all these sets, denoted as $\mathcal{X} = \mathcal{X}^1 \uplus \cdots \uplus \mathcal{X}^n$, has the multi-object density [49, Section 4.2.3]

$$f(\mathcal{X}) = \sum_{\mathcal{X}^1 \uplus \cdots \uplus \mathcal{X}^n = \mathcal{X}} \prod_{i=1}^{n} f^i(\mathcal{X}^i), \tag{5.2}$$

where the summation is taken over all mutually disjoint (and possibly empty) sets $\mathcal{X}^1, \ldots, \mathcal{X}^n$, whose union is $\mathcal{X}$. This essentially means that we obtain one term for every possible way that $\mathcal{X}$ can be generated.

Cardinality distribution

The cardinality distribution of an RFS with multi-object density $f(\mathcal{X})$ is given by [49, Section 4.2.6]

$$p(n) = \frac{1}{n!} \int f(\{\boldsymbol{x}^1, \boldsymbol{x}^2, \ldots, \boldsymbol{x}^n\}) \mathrm{d}\boldsymbol{x}^1 \ldots \mathrm{d}\boldsymbol{x}^n, \tag{5.3}$$

where $p(n)$ represents the probability of $|\mathcal{X}| = n$. This function serves as a probability mass function capturing the distribution of the cardinality.

5.3 Important RFSs

In this section, various standard types of RFSs are introduced.

5.3.1 Poisson point process

In a PPP, all elements are independently and identically distributed according to a spatial density $p(\boldsymbol{x})$, and the cardinality of the set follows a Poisson distribution with a mean $\mu \geq 0$. The multi-object density for a PPP $\mathcal{X} = \{\boldsymbol{x}^1, \ldots, \boldsymbol{x}^n\}$ is expressed as [49, Section 4.3.1]

$$f_{\mathrm{PPP}}(\mathcal{X}) = e^{-\int \lambda(\boldsymbol{x}) \mathrm{d}\boldsymbol{x}} \prod_{i=1}^{n} \lambda(\boldsymbol{x}^i), \tag{5.4}$$

where $\lambda(\boldsymbol{x}) = \mu p(\boldsymbol{x})$ denotes the intensity function, and n signifies the cardinality of $\mathcal{X}$. From (5.4), we can observe that a PPP can be characterized by its intensity function $\lambda(\boldsymbol{x})$.

5.3.2 Bernoulli process

In a Bernoulli process, the cardinality of the set follows a Bernoulli distribution with a mean $r \in [0, 1]$. This implies that a Bernoulli process can have at most one element, and the potential element follows a spatial density $p(\boldsymbol{x})$. Consequently, the multi-object density for a Bernoulli process $\mathcal{X}$ is expressed as [49, Section 4.3.3]

$$f_{\mathrm{B}}(\mathcal{X}) = \begin{cases} 1 - r & \mathcal{X} = \varnothing \\ r p(\boldsymbol{x}) & \mathcal{X} = \{\boldsymbol{x}\} \\ 0 & \text{otherwise,} \end{cases} \tag{5.5}$$

where r is the mean of the Bernoulli distribution, which also refers to the existence probability of the Bernoulli process. A higher r suggests a higher likelihood of having an element, while a lower r implies a lower likelihood. From (5.5), we can observe that a Bernoulli process can be parameterized by r and $p(\boldsymbol{x})$.

5.3.3 Multi-Bernoulli

An multi-Bernoulli (MB) RFS $\mathcal{X}$ corresponds to the union of a finite number n of independent Bernoulli processes, expressed as $\mathcal{X} = \mathcal{X}^1 \uplus \cdots \uplus \mathcal{X}^n$, where $\mathcal{X}^i, i \in \{1, \ldots, n\}$ signifies a Bernoulli process. Utilizing the convolution formula, the multi-object density for an MB RFS $\mathcal{X}$ is provided by [49, Section 4.3.4]

$$f_{\mathrm{MB}}(\mathcal{X}) = \sum_{\mathcal{X}^1 \uplus \cdots \uplus \mathcal{X}^n = \mathcal{X}} \prod_{i=1}^{n} f_{\mathrm{B}}^i(\mathcal{X}^i), \tag{5.6}$$

where $f_{\mathrm{B}}^{i}(\mathcal{X}^{i})$ denotes the multi-object density for the i-th Bernoulli process $\mathcal{X}^{i}$, parameterized by r^{i} and $p^{i}(\boldsymbol{x})$. Therefore, an MB RFS can be parameterized by a set of parameters $\{(r^{1}, p^{1}(\boldsymbol{x})), \ldots, (r^{n}, p^{n}(\boldsymbol{x}))\}$.

5.3.4 Multi-Bernoulli mixture

An multi-Bernoulli mixture (MBM) RFS is characterized as a weighted sum of a finite number J of MB RFSs. The multi-object density for an MBM RFS $\mathcal{X}$ is defined by [103]

$$f_{\mathrm{MBM}}(\mathcal{X}) = \sum_{j=1}^{J} \omega^{j} \sum_{\mathcal{X}^{1} \uplus \cdots \uplus \mathcal{X}^{n} = \mathcal{X}} \prod_{i=1}^{n} f_{\mathrm{B}}^{j,i}(\mathcal{X}^{i}), \tag{5.7}$$

where ω^{j} represents the weight for the j-th MB with $\omega^{j} \geq 0$ and $\sum_{j=1}^{J} \omega^{j} = 1$, and $f_{\mathrm{B}}^{j,i}(\mathcal{X}^{i})$ denotes the multi-object density for the i-th Bernoulli process of the j-th MB with $i \in \{1, \ldots, n\}$ and $j \in \{1, \ldots, J\}$, parameterized by $r^{j,i}$ and $p^{j,i}(\boldsymbol{x})$. Thus, an MBM RFS can be parameterized by a set of parameters $\{\omega^{j}, \{(r^{j,i}, p^{j,i}(\boldsymbol{x}))\}_{i \in \{1,\ldots,n\}}\}_{j \in \{1,\ldots,J\}}$. It is important to note that the weights ω^{j} typically correspond to the probabilities of different DA sequences [51, 103].

5.3.5 Poisson multi-Bernoulli mixture

A PMBM RFS $\mathcal{X}$ is constructed as to the union of two disjoint RFS, denoted as $\mathcal{X}_{\mathrm{U}}$ and $\mathcal{X}_{\mathrm{D}}$, such that $\mathcal{X} = \mathcal{X}_{\mathrm{U}} \uplus \mathcal{X}_{\mathrm{D}}$. The RFSs $\mathcal{X}_{\mathrm{U}}$ and $\mathcal{X}_{\mathrm{D}}$ are modeled as a PPP RFS and an MBM RFS, respectively. Utilizing the convolution formula, the multi-object density for the PMBM RFS $\mathcal{X}$ is expressed as [51, 103, 104]

$$\begin{aligned} f(\mathcal{X}) &= \sum_{\mathcal{X}_{\mathrm{U}} \uplus \mathcal{X}_{\mathrm{D}} = \mathcal{X}} f_{\mathrm{P}}(\mathcal{X}_{\mathrm{U}}) f_{\mathrm{MBM}}(\mathcal{X}_{\mathrm{D}}) \\ &= e^{-\int \lambda(\boldsymbol{x}) d\boldsymbol{x}} \sum_{\mathcal{X}_{\mathrm{U}} \uplus \mathcal{X}_{\mathrm{D}} = \mathcal{X}} \prod_{i'=1}^{|\mathcal{X}_{\mathrm{U}}|} \lambda(\boldsymbol{x}^{i'}) \sum_{j=1}^{J} \omega^{j} \sum_{\mathcal{X}^{1} \uplus \cdots \uplus \mathcal{X}^{n} = \mathcal{X}_{\mathrm{D}}} \prod_{i=1}^{n} f_{\mathrm{B}}^{j,i}(\mathcal{X}^{i}), \end{aligned} \tag{5.8}$$

which can be parameterized by $\lambda(\boldsymbol{x})$ and $\{\omega^{j}, \{(r^{j,i}, p^{j,i}(\boldsymbol{x}))\}_{i \in \{1,\ldots,n\}}\}_{j \in \{1,\ldots,J\}}$. If only one mixture term is present, the PMBM reduces to a Poisson multi-Bernoulli (PMB). In Fig. 5.1, an illustrative depiction of a PMBM RFS with two MBs is presented.

5.4 Evaluation matrices

It is essential to assess the dissimilarity between two sets. For instance, when evaluating the mapping performance of a SLAM algorithm, one may seek to quantify the variance between the estimated map and the ground-truth map. This section introduces two common matrices for assessing disparities between two sets.

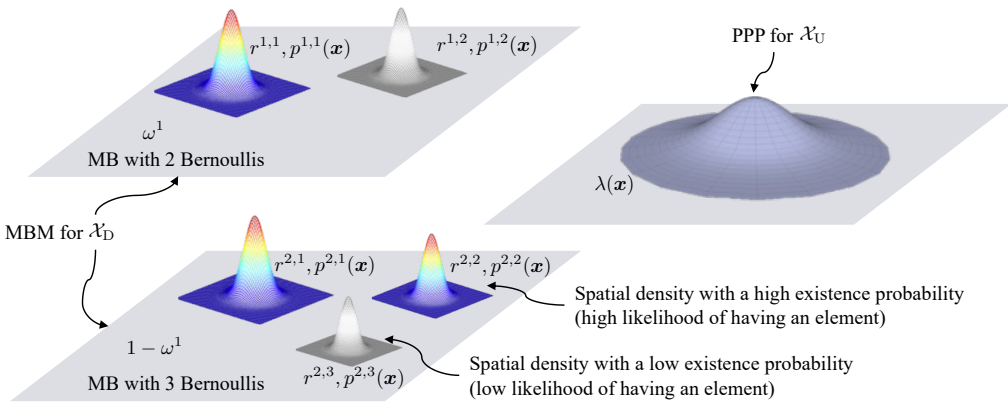

Figure 5.1: Illustrative presentation of a PMBM RFS with two MBs. The intensity of the PPP is denoted by $\lambda(\boldsymbol{x})$. The first MB carries a weight of ω^1, and comprises two Bernoulli processes with existence probabilities and spatial densities denoted as $(r^{1,1}, p^{1,1}(\boldsymbol{x}))$ and $(r^{1,2}, p^{1,2}(\boldsymbol{x}))$, respectively. The second MB has a weight of $1-\omega^1$, and encompasses three Bernoulli processes with their existence probabilities and spatial densities denoted as $(r^{2,1}, p^{2,1}(\boldsymbol{x}))$, $(r^{2,2}, p^{2,2}(\boldsymbol{x}))$ and $(r^{2,3}, p^{2,3}(\boldsymbol{x}))$, respectively. A Bernoulli process with a high existence probability is portrayed with intense color saturation, signifying a high likelihood of containing an element. Conversely, a Bernoulli process with a low existence probability is depicted with lower color saturation, indicating a lower likelihood of containing an element.

OSPA

The optimal subpattern assignment (OSPA) metric between $\mathcal{X}$ and $\mathcal{Y}$ is defined as [105, 106]

$$d_{\mathrm{OSPA}}(\mathcal{X}, \mathcal{Y}) = \begin{cases} \left(\frac{1}{|\mathcal{Y}|} \left(\min_{\pi \in \Pi_{|\mathcal{Y}|}} \sum_{i=1}^{|\mathcal{X}|} d^{(q_c)}(\boldsymbol{x}_i, \boldsymbol{y}_{\pi(i)})^{q_p} + q_c^{q_p} (|\mathcal{Y}| - |\mathcal{X}|) \right) \right)^{\frac{1}{q_p}} & |\mathcal{X}| \leq |\mathcal{Y}| \\ \left(\frac{1}{|\mathcal{X}|} \left(\min_{\pi \in \Pi_{|\mathcal{X}|}} \sum_{i=1}^{|\mathcal{Y}|} d^{(q_c)}(\boldsymbol{x}_i, \boldsymbol{y}_{\pi(i)})^{q_p} + q_c^{q_p} (|\mathcal{X}| - |\mathcal{Y}|) \right) \right)^{\frac{1}{q_p}} & |\mathcal{X}| > |\mathcal{Y}| \\ 0 & \mathcal{X} = \mathcal{Y} = \varnothing \end{cases}, \tag{5.9}$$

where $q_c > 0$ denotes the cut-off metric, signifying the maximum distance allowable for matching two elements from different sets, $1 \leq q_p < \infty$ denotes the exponent factor, with a higher q_p implying a greater penalty for outliers, $\Pi_\star$ indicates the set of all permutations of the integers $\{1, \ldots, |\star|\}$, and any element $\pi \in \Pi_\star$ is a sequence represented as $(\pi(1), \ldots, \pi(|\star|))$, and $d^{(q_c)}(\boldsymbol{x}_i, \boldsymbol{y}_{\pi(i)})$ refers to the metric between $\boldsymbol{x}_i$ and $\boldsymbol{y}_{\pi(i)}$ cut off at q_c, defined as

$$d^{(q_c)}(\boldsymbol{x}_i, \boldsymbol{y}_{\pi(i)}) = \min(d(\boldsymbol{x}_i, \boldsymbol{y}_{\pi(i)}), q_c). \tag{5.10}$$

with $d(\boldsymbol{x}_i, \boldsymbol{y}_{\pi(i)})$ denoting the Lq_p distance between $\boldsymbol{x}_i$ and $\boldsymbol{y}_{\pi(i)}$. The OSPA metric contains two parts (considering the case $|\mathcal{X}| \leq |\mathcal{Y}|$ as an example):

- Normalized state errors: $\frac{1}{|\mathcal{Y}|} \min_{\pi \in \Pi_{|\mathcal{Y}|}} \sum_{i=1}^{|\mathcal{X}|} d^{(q_c)}(\boldsymbol{x}_i, \boldsymbol{y}_{\pi(i)})^{q_p}$. It considers the state errors for elements in the smallest set within the optimal subpattern assignment.

- Normalized cardinality error: $\frac{1}{|\mathcal{Y}|} q_c^{q_p} (|\mathcal{Y}| - |\mathcal{X}|)$. It accounts for the cardinality mismatch of the two target sets, penalized at the maximal distance.

GOSPA

The generalized optimal subpattern assignment (GOSPA) metric between $\mathcal{X}$ and $\mathcal{Y}$ is defined as [107]

$$d_{\text{GOSPA}}(\mathcal{X}, \mathcal{Y}) = \begin{cases} \left(\min_{\pi \in \Pi_{|\mathcal{Y}|}} \sum_{i=1}^{|\mathcal{X}|} d^{(q_c)}(\boldsymbol{x}_i, \boldsymbol{y}_{\pi(i)})^{q_p} + \frac{q_c^{q_p}}{q_a} (|\mathcal{Y}| - |\mathcal{X}|) \right)^{\frac{1}{q_p}} & |\mathcal{X}| \leq |\mathcal{Y}| \\ \left(\min_{\pi \in \Pi_{|\mathcal{X}|}} \sum_{i=1}^{|\mathcal{Y}|} d^{(q_c)}(\boldsymbol{x}_i, \boldsymbol{y}_{\pi(i)})^{q_p} + \frac{q_c^{q_p}}{q_a} (|\mathcal{Y}| - |\mathcal{X}|) \right)^{\frac{1}{q_p}} & |\mathcal{X}| > |\mathcal{Y}| \\ 0 & \mathcal{X} = \mathcal{Y} = \varnothing \end{cases}. \tag{5.11}$$

In contrast to the OSPA in (5.10), the notable distinctions include the absence of the normalized factor $\max(|\mathcal{X}|, |\mathcal{Y}|)$, and the introduction of the cardinality penalty factor $2 \geq q_a > 0$, which governs the penalty for cardinality mismatch. The key characteristic of the GOSPA metric is that, for $q_a = 2$, the metric can be expressed as

$$d_{\text{GOSPA}}(\mathcal{X}, \mathcal{Y}) = \left(\min_{\gamma \in \Gamma} \sum_{(i,j) \in \gamma} d^{(q_c)}(\boldsymbol{x}_i, \boldsymbol{y}_j)^{q_p} + \frac{q_c^{q_p}}{2} (|\mathcal{X}| - |\gamma| + |\mathcal{Y}| - |\gamma|) \right)^{\frac{1}{q_p}}, \tag{5.12}$$

where γ represents an assignment set between $\mathcal{X}$ and $\mathcal{Y}$, and Γ is the set of all potential assignment sets. Assuming $\mathcal{Y}$ is the estimation of $\mathcal{X}$, we can break down (5.12) into the following components:

- The sum of state errors for detected elements: $\min_{\gamma \in \Gamma} \sum_{(i,j) \in \gamma} d^{(q_c)}(\boldsymbol{x}_i, \boldsymbol{y}_j)^{q_p}$. It considers all state errors between each pair of assigned states within the optimal subpattern assignment.

- Misdetection error: $\frac{q_c^{q_p}}{2} (|\mathcal{X}| - |\gamma|)$. It represents the penalty for true elements in $\mathcal{X}$ having no corresponding estimates in $\mathcal{Y}$.

- False alarm error: $\frac{q_c^{q_p}}{2} (|\mathcal{Y}| - |\gamma|)$. It indicates the penalty for estimates in $\mathcal{Y}$ having no corresponding true elements in $\mathcal{X}$.

These three error types are crucial and more straightforward in the MOT problem compared to the errors involving elements in the smallest set and cardinality mismatch. In this context, elements can be left unassigned, and only nearby elements are assigned to each other. Therefore, the GOSPA metric encourages systems to minimize false alarms and misdetections. For instance, adding false alarms does not necessarily increase the OSPA metric, but it consistently increases the GOSPA metric. Moreover, as shown in [108], the negative effects observed in the optimal estimation of multiple objects with the OSPA metric do not apply to the GOSPA metric.

CHAPTER 6

SLAM with random finite sets

As outlined in Section 4.2.4, the solution to the SLAM problem can be approached through RFS theory, giving rise to RFS-SLAM. This chapter presents the RFS-SLAM framework, delves into multi-object measurement models, and introduces two implementations of RFS-SLAM.

6.1 RFS-SLAM

The distinctive feature of RFS-SLAM, setting it apart from other SLAM approaches, lies in the modeling of both landmarks in the environment and received measurements as RFSs. To obtain the joint posterior density of the UE trajectory and the map $f(\boldsymbol{s}_{1:k}, \mathcal{X}|\mathcal{Z}_{1:k}, \boldsymbol{u}_{1:k}, \boldsymbol{s}_0)$, given the initial UE state $\boldsymbol{s}_0$, measurements $\mathcal{Z}_{1:k}$ and controls $\boldsymbol{u}_{1:k}$ up to the current time instant k, we can follow the prediction and update steps of the Bayesian filtering recursion applied with RFSs, as described in [91]

$$f(\boldsymbol{s}_{1:k}, \mathcal{X}|\mathcal{Z}_{1:k-1}, \boldsymbol{u}_{1:k}, \boldsymbol{s}_0) = f(\boldsymbol{s}_k|\boldsymbol{s}_{k-1}, \boldsymbol{u}_k) f(\boldsymbol{s}_{1:k-1}, \mathcal{X}|\mathcal{Z}_{1:k-1}, \boldsymbol{u}_{1:k-1}, \boldsymbol{s}_0), \tag{6.1}$$

$$f(\boldsymbol{s}_{1:k}, \mathcal{X}|\mathcal{Z}_{1:k}, \boldsymbol{u}_{1:k}, \boldsymbol{s}_0) = \frac{g(\mathcal{Z}_k|\mathbf{s}_k, \mathcal{X}) f(\boldsymbol{s}_{1:k}, \mathcal{X}|\mathcal{Z}_{1:k-1}, \boldsymbol{u}_{1:k}, \boldsymbol{s}_0)}{p(\mathcal{Z}_{1:k}|\mathcal{Z}_{1:k-1}, \boldsymbol{s}_0)}, \tag{6.2}$$

respectively, where $g(\mathcal{Z}_k|\mathbf{s}_k, \mathcal{X})$ denotes the RFS likelihood function, which will be introduced in the next section, and $p(\mathcal{Z}_{1:k}|\mathcal{Z}_{1:k-1}, \boldsymbol{s}_0)$ serves as a normalization constant and is given by

$$p(\mathcal{Z}_{1:k}|\mathcal{Z}_{1:k-1}, \boldsymbol{s}_0) = \int \int g(\mathcal{Z}_k|\mathbf{s}_k, \mathcal{X}) f(\boldsymbol{s}_{1:k}, \mathcal{X}|\mathcal{Z}_{1:k-1}, \boldsymbol{u}_{1:k}, \boldsymbol{s}_0) \mathrm{d}\boldsymbol{s}_{1:k} \delta\mathcal{X}. \tag{6.3}$$

It is worth noting that, mathematically, there is also a map prediction in the prediction step. However, as all landmarks remain static, we omit the map prediction in (6.1).

6.2 Multi-object measurement models

In contrast to the conventional SLAM frameworks, where measurements are represented as vectors, the RFS-SLAM framework represents measurements as RFSs. In this framework, each measurement can be a genuine observation originating from a landmark or a clutter measurement without a corresponding source landmark. Landmarks, in turn, can either be correctly detected with at least one measurement or go undetected with no associated measurement. The measurement model needs to account for both types of measurements and the status of landmarks. Thus, the RFS likelihood function, denoted as $g(\mathcal{Z}_k|\boldsymbol{s}_k, \mathcal{X})$, is expressed as [51]

$$g(\mathcal{Z}_k|\boldsymbol{s}_k, \mathcal{X}) = e^{-\int c(\boldsymbol{z})\mathrm{d}\boldsymbol{z}} \sum_{\mathcal{Z}_k^c \uplus \mathcal{Z}_k^1 \ldots \uplus \mathcal{Z}_k^{|\mathcal{X}|} = \mathcal{Z}_k} \prod_{\boldsymbol{z}\in\mathcal{Z}^c} c(\boldsymbol{z}) \prod_{i=1}^{|\mathcal{X}|} \ell(\mathcal{Z}_k^i|\boldsymbol{s}_k, \boldsymbol{x}^i). \tag{6.4}$$

The interpretation of (6.4) involves partitioning the measurement set $\mathcal{Z}_k$ into a collection of disjoint subsets based on their sources, represented as $\mathcal{Z}_k = \mathcal{Z}_k^c \uplus \mathcal{Z}_k^1 \ldots \uplus \mathcal{Z}_k^{|\mathcal{X}|}$. Here, $\mathcal{Z}_k^c$ denotes the set of all clutter measurements, and $\mathcal{Z}_k^i$ is the set of all measurements originating from the i-th landmark $\boldsymbol{x}^i$, which could be empty if the i-th landmark is undetected. Clutter measurements are modeled as a PPP RFS with clutter intensity $c(\boldsymbol{z})$, and $\ell(\mathcal{Z}_k^i|\boldsymbol{s}_k, \boldsymbol{x}^i)$ is the likelihood of the set of all measurements from $\boldsymbol{x}^i$.

6.2.1 Point object model

In the point object model, we make the assumption that each landmark can produce at most one measurement per time step, and there are no instances of two measurements originating from the same landmark within a given time step. In other words, a landmark can be either misdetected or detected with only one measurement. Consequently, the likelihood function for a point object $\boldsymbol{x}^i$ is generally given by [49, Section 5.7]

$$\ell(\mathcal{Z}_k^i|\boldsymbol{s}_k, \boldsymbol{x}^i) = \begin{cases} 1 - p_{\mathrm{D}}(\boldsymbol{x}^i, \boldsymbol{s}_k) & \mathcal{Z}_k^i = \varnothing, \\ p_{\mathrm{D}}(\boldsymbol{x}^i, \boldsymbol{s}_k) f(\boldsymbol{z}|\boldsymbol{x}^i, \boldsymbol{s}_k) & \mathcal{Z}_k^i = \{\boldsymbol{z}\}, \\ 0 & \text{otherwise}, \end{cases} \tag{6.5}$$

where $p_{\mathrm{D}}(\boldsymbol{x}^i, \boldsymbol{s}_k) \in [0, 1]$ denotes the detection probability, and $f(\boldsymbol{z}|\boldsymbol{x}^i, \boldsymbol{s}_k)$ is the likelihood, for example, can be given by (2.3). The first entry in (6.5) signifies the misdetection of $\boldsymbol{x}^i$, while the second entry corresponds to the successful detection of $\boldsymbol{x}^i$. It is evident that (6.5) describes a Bernoulli process. By substituting (6.5) into (6.4), we obtain a PMB RFS.

6.2.2 Extended object model

In the extended object model, a single landmark can generate multiple measurements per time step. For instance, a wall may reflect and diffuse downlink signals from the BS, resulting in more than one path. Similar to (6.5), the likelihood function for an extended object $\boldsymbol{x}^i$ is typically expressed as [49, Section 21.2]

$$\ell(\mathcal{Z}_k^i|\boldsymbol{s}_k,\boldsymbol{x}^i) = \begin{cases} 1 - p_{\mathrm{D}}(\boldsymbol{x}^i,\boldsymbol{s}_k) + p_{\mathrm{D}}(\boldsymbol{x}^i,\boldsymbol{s}_k) f(\mathcal{Z}_k^i|\boldsymbol{x}^i,\boldsymbol{s}_k) & \mathcal{Z}_k^i = \varnothing, \\ p_{\mathrm{D}}(\boldsymbol{x}^i,\boldsymbol{s}_k) f(\mathcal{Z}_k^i|\boldsymbol{x}^i,\boldsymbol{s}_k) & \mathcal{Z}_k^i \neq \varnothing, \end{cases} \tag{6.6}$$

where $f(\mathcal{Z}_k^i|\boldsymbol{x}^i,\boldsymbol{s}_k)$ denotes the model for measurements generated by the landmark given $\boldsymbol{x}^i$ and $\boldsymbol{s}_k$. The specific form of this model, such as being modeled as a PPP [104, 109], needs to be determined based on the particular problem. The first entry in (6.6) consists of two terms: $1-p_{\mathrm{D}}(\boldsymbol{x}^i,\boldsymbol{s}_k)$ representing the case where the landmark is not detected, and $p_{\mathrm{D}}(\boldsymbol{x}^i,\boldsymbol{s}_k) f(\mathcal{Z}_k^i = \varnothing|\boldsymbol{x}^i,\boldsymbol{s}_k)$ representing the case where the landmark does not generate any measurement.

6.3 Implementations of RFS-SLAM

This section presents two implementations of RFS-SLAM.

6.3.1 Rao-Blackwellized particle-based RFS

One of the key features of the SLAM problem is that landmarks exhibit conditional independence when the map is conditioned on the UE trajectory. This characteristic makes it natural to employ RBPF solutions. Consequently, RFS-SLAM can be accomplished through Rao-Blackwellized particle (RBP) implementation. In the RBP implementation, the joint posterior density $f(\boldsymbol{s}_{1:k},\mathcal{X}|\mathcal{Z}_{1:k},\boldsymbol{u}_{1:k},\boldsymbol{s}_0)$ is factorized into [91]

$$f(\boldsymbol{s}_{1:k},\mathcal{X}|\mathcal{Z}_{1:k},\boldsymbol{u}_{1:k},\boldsymbol{s}_0) = f(\boldsymbol{s}_{1:k}|\mathcal{Z}_{1:k},\boldsymbol{u}_{1:k},\boldsymbol{s}_0) f(\mathcal{X}|\mathcal{Z}_{1:k},\boldsymbol{s}_{0:k}). \tag{6.7}$$

Then, the recursion for the joint posterior density $f(\boldsymbol{s}_{1:k},\mathcal{X}|\mathcal{Z}_{1:k},\boldsymbol{u}_{1:k},\boldsymbol{s}_0)$ is equivalent to jointly propagating the posterior density of the UE trajectory, $f(\boldsymbol{s}_{1:k}|\mathcal{Z}_{1:k},\boldsymbol{u}_{1:k},\boldsymbol{s}_0)$, and the posterior density of the map conditioned on the UE trajectory, $f(\mathcal{X}|\mathcal{Z}_{1:k},\boldsymbol{s}_{0:k})$.

In accordance with (6.1)–(6.2), the posterior density of the UE trajectory undergoes an update given by

$$f(\boldsymbol{s}_{1:k}|\mathcal{Z}_{1:k},\boldsymbol{u}_{1:k},\boldsymbol{s}_0) = \frac{f(\boldsymbol{s}_{1:k}|\mathcal{Z}_{1:k-1},\boldsymbol{u}_{1:k},\boldsymbol{s}_0) p(\mathcal{Z}_k|\mathcal{Z}_{1:k-1},\boldsymbol{s}_{0:k})}{p(\mathcal{Z}_k|\mathcal{Z}_{1:k-1},\boldsymbol{s}_0)}, \tag{6.8}$$

where $f(\boldsymbol{s}_{1:k}|\mathcal{Z}_{1:k-1},\boldsymbol{u}_{1:k},\boldsymbol{s}_0)$ represents the predicted UE trajectory density and is given by

$$f(\boldsymbol{s}_{1:k}|\mathcal{Z}_{1:k-1},\boldsymbol{u}_{1:k},\boldsymbol{s}_0) = f(\boldsymbol{s}_{1:k-1}|\mathcal{Z}_{1:k-1},\boldsymbol{u}_{1:k-1},\boldsymbol{s}_0) f(\boldsymbol{s}_k|\boldsymbol{u}_k,\boldsymbol{s}_{k-1}), \tag{6.9}$$

while the posterior density of the map $f(\mathcal{X}|\mathcal{Z}_{1:k}, \boldsymbol{s}_{0:k})$ is updated according to

$$f(\mathcal{X}|\mathcal{Z}_{1:k}, \boldsymbol{s}_{0:k}) = \frac{f(\mathcal{X}|\mathcal{Z}_{1:k-1}, \boldsymbol{s}_{0:k}) g(\mathcal{Z}_k|\boldsymbol{s}_k, \mathcal{X})}{p(\mathcal{Z}_k|\mathcal{Z}_{1:k-1}, \boldsymbol{s}_{0:k})}, \tag{6.10}$$

where $f(\mathcal{X}|\mathcal{Z}_{1:k-1}, \boldsymbol{s}_{0:k}) = f(\mathcal{X}|\mathcal{Z}_{1:k-1}, \boldsymbol{s}_{0:k-1})$, as the landmarks remain static. The normalization constant for the map $p(\mathcal{Z}_k|\mathcal{Z}_{1:k-1}, \boldsymbol{s}_{0:k})$ is given by

$$p(\mathcal{Z}_k|\mathcal{Z}_{1:k-1}, \boldsymbol{s}_{0:k}) = \int f(\mathcal{X}|\mathcal{Z}_{1:k-1}, \boldsymbol{s}_{0:k}) g(\mathcal{Z}_k|\boldsymbol{s}_k, \mathcal{X}) \delta\mathcal{X}. \tag{6.11}$$

By adopting the RBP approach [110, Chapter 7.1], the posterior density of the UE trajectory can be approximated using a weighted set of N particles

$$f(\boldsymbol{s}_{1:k}|\mathcal{Z}_{1:k}, \boldsymbol{u}_{1:k}, \boldsymbol{s}_0) \approx \sum_{n=1}^{N} w_k^{(n)} \delta\left(\boldsymbol{s}_{1:k} - \boldsymbol{s}_{1:k}^{(n)}\right), \tag{6.12}$$

where $\delta(\cdot)$ represents the Dirac delta distribution, $\boldsymbol{s}_{1:k}^{(n)}$ denotes the n-th particle, N is the total number of particles, and $w_k^{(n)}$ is the associated weight to the n-th particle. It is crucial to note that a sufficiently large number of particles are required to adequately cover the properties of the sampled states. Hence, N is typically a large number, increasing exponentially with the dimension of the sampled state. For each particle, there is a map conditioned on it, modeled as an RFS with the multi-object density $f(\mathcal{X}|\mathcal{Z}_{1:k}, \boldsymbol{s}_{0:k}^{(n)})$. Therefore, in RFS-SLAM, the posterior RFS-SLAM density is represented by a weighted set of N particles $\{w_k^{(n)}, \boldsymbol{s}_{0:k}^{(n)}, f(\mathcal{X}|\mathcal{Z}_{1:k}, \boldsymbol{s}_{0:k}^{(n)})\}_{n=1}^{N}$. It is essential to emphasize that each particle encapsulates a single hypothesis of the UE trajectory and the associated map. Moreover, a higher particle weight signifies a higher likelihood for the corresponding hypothesis. The subsequent discussion elucidates how these particle components are computed at time step k.

Draw particles

Ideally, particles should be drawn from the posterior $f(\boldsymbol{s}_{1:k}|\mathcal{Z}_{1:k}, \boldsymbol{u}_{1:k}, \boldsymbol{s}_0)$. However, due to the complex functional form of the posterior, directly obtaining particles from it is usually impractical. Instead, an approximate distribution known as the importance density is used, denoted as $q(\boldsymbol{s}_k|\boldsymbol{s}_{0:k-1}^n, \mathcal{Z}_{1:k}, \boldsymbol{u}_{1:k})$, from which particles can be easily drawn [111, Section 2.5]. For each particle, we perform

$$\boldsymbol{s}_k^{(n)} \sim q(\boldsymbol{s}_k|\boldsymbol{s}_{0:k-1}^{(n)}, \mathcal{Z}_{1:k}, \boldsymbol{u}_{1:k}). \tag{6.13}$$

A common choice for the importance density is the transition density $f(\boldsymbol{s}_k|\boldsymbol{u}_k, \boldsymbol{s}_{k-1})$, although there are various other methods for selecting the importance density.

Map update for each particle

In RBP-based RFS-SLAM, each particle encompasses a UE trajectory $\boldsymbol{s}_{0:k}^{(n)}$ and a map conditioned on the trajectory $f(\mathcal{X}|\mathcal{Z}_{1:k}, \boldsymbol{s}_{0:k}^{(n)})$, where the map is represented as an RFS.

The specific form of the map representation may vary; for instance, the map can be modeled as a PPP, yielding a probability hypothesis density (PHD) filter for the map [112], or as a PMBM, resulting in a PMBM filter for the map [51]. Regardless of the chosen RFS to model the map, the update for each map can be expressed as

$$f(\mathcal{X}|\mathcal{Z}_{1:k}, \boldsymbol{s}_{0:k}^{(n)}) = \frac{f(\mathcal{X}|\mathcal{Z}_{1:k-1}, \boldsymbol{s}_{0:k}^{(n)}) g(\mathcal{Z}_k|\boldsymbol{s}_k^{(n)}, \mathcal{X})}{p(\mathcal{Z}_k|\mathcal{Z}_{1:k-1}, \boldsymbol{s}_{0:k}^{(n)})}. \tag{6.14}$$

However, the utilization of different RFSs leads to distinct update details, DA solutions, and, naturally, varying outcomes.

Weight update

The update of each particle weight is carried out according to [80, Section 11.3]

$$w_k^{(n)} \propto w_{k-1}^{(n)} \frac{p(\mathcal{Z}_k|\mathcal{Z}_{1:k-1}, \boldsymbol{s}_{0:k}^{(n)}) f(\boldsymbol{s}_k^{(n)}|\boldsymbol{s}_{k-1}^{(n)}, \boldsymbol{u}_k)}{q(\boldsymbol{s}_k^{(n)}|\boldsymbol{s}_{0:k-1}^{(n)}, \mathcal{Z}_{1:k}, \boldsymbol{u}_{1:k})}. \tag{6.15}$$

The computation of the normalization constant $p(\mathcal{Z}_k|\mathcal{Z}_{1:k-1}, \boldsymbol{s}_{0:k}^{(n)})$ differs based on the chosen RFS. When the transition density is utilized as the importance density $q(\cdot)$, the updated weight is simplified to

$$w_k^{(n)} \propto w_{k-1}^{(n)} p(\mathcal{Z}_k|\mathcal{Z}_{1:k-1}, \boldsymbol{s}_{0:k}^{(n)}). \tag{6.16}$$

After updating the weight for each particle, the weights are normalized

$$w_k^{(n)} = \frac{w_k^{(n)}}{\sum_{n=1}^{N} w_k^{(n)}}. \tag{6.17}$$

Resampling is performed at each time step if the effective sample size is below a predetermined threshold, denoted as the index indicating the "effective" number of particles and used for monitoring the need for resampling. It can be estimated from the variance of the particle weights [113, Section 8.6]

$$n_{\text{ESS}} = \frac{1}{\sum_{n=1}^{N} (w_k^{(n)})^2}. \tag{6.18}$$

A typical resampling process involves drawing N samples from the discrete distribution defined by the weights $\{w_k^{(n)}\}_{n=1}^{N}$ and replacing the old sample set with this new one, setting all weights to $1/N$ [80, Section 11.4].

RBP-based solutions often exhibit robust performance by keeping cross-correlation between the UE trajectory and the map through particles. However, the effectiveness of these solutions comes at the cost of requiring numerous particles to accurately propagate the posterior over time. The requirement for the number of particles increases exponentially with the UE state dimension. Moreover, for each particle, an RFS filter is employed to estimate the map. Consequently, RBP-based approaches often face considerable complexity, rendering them impractical for real-time applications.

6.3.2 Marginalization

As discussed in Section 6.3.1, RBP-based RFS-SLAM approaches face challenges in terms of high complexity, primarily stemming from the necessity of a large number of particles. To mitigate this complexity, marginal posterior densities $f(\mathbf{s}_k|\mathcal{Z}_{1:k}, \boldsymbol{u}_{1:k})$ and $f(\mathcal{X}|\mathcal{Z}_{1:k})$ are monitored at each time step, rather than maintaining the entire SLAM posterior through particles [100]. This pragmatic approach involves a trade-off, as it results in the loss of correlations between the UE trajectory and the map, but it allows for a significant reduction in computational complexity. In the following, the computation of these two marginal posteriors at time step k is discussed.

Joint UE and map prediction and update

The crux of marginalization-based approaches lies in efficiently approximating the joint posterior $f(\boldsymbol{s}_k, \mathcal{X}|\mathcal{Z}_{1:k}, \boldsymbol{u}_{1:k})$ through two marginal posterior densities. Achieving this entails the joint update of the UE and map by leveraging $g(\mathcal{Z}_k|\mathbf{s}_k, \mathcal{X})$. However, this presents a challenge due to the disparate nature of $\mathcal{X}$ as an RFS and $\boldsymbol{s}_k$ as a random vector. Additionally, the DA between the measurement $\mathcal{Z}_k$ and landmarks $\mathcal{X}$ remains unknown. To address this, one can attempt to vectorize the problem during the update, employ low-complexity methods (e.g., based on linearization) to solve the vectorized problem, and subsequently reconstruct the appropriate multi-object density from the results.

Marginalization

Then, the two marginal posteriors can be derived by marginalizing out the rest state from the full SLAM posterior, given by

$$f(\mathbf{s}_k|\mathcal{Z}_{1:k}, \boldsymbol{u}_{1:k}) = \int f(\boldsymbol{s}_k, \mathcal{X}|\mathcal{Z}_{1:k}, \boldsymbol{u}_{1:k})\delta\mathcal{X}, \tag{6.19}$$

$$f(\mathcal{X}|\mathcal{Z}_{1:k}) = \int f(\boldsymbol{s}_k, \mathcal{X}|\mathcal{Z}_{1:k}, \boldsymbol{u}_{1:k})\mathrm{d}\mathbf{s}_k. \tag{6.20}$$

It is important to note that marginalizing out the UE state introduces correlations among landmarks. To maintain the RFS format, we drop these correlations by assuming that all landmarks are independent, although this introduces a loss of information.

Marginalization-based approaches exhibit relatively low complexity and have demonstrated satisfactory performance in certain scenarios, as exemplified in [Paper B]. However, by discarding the cross-correlation between the UE and the map, as well as among all landmarks, these approaches come at the cost of sacrificing SLAM performance and robustness. Additionally, the measurement function in the joint update often involves high non-linearity, necessitating careful consideration when employing linearization methods.

6.3.3 Discussions

It is noteworthy that, despite the similarities in appearance between the equations presented in Section 6.3.1 and Section 6.3.2 to vector-based equations commonly used in the

SLAM literature, they are inherently different. This distinction arises from the utilization of RFSs in this thesis, which possess entirely different statistical properties compared to random vectors. Consequently, the derivation of the posterior involves fundamental differences. Therefore, it is crucial to recognize that the prediction and update details of traditional vector-based methods cannot be directly applied to compute the RFS-based posterior. For a comprehensive understanding of these distinctions, we provide the prediction and update details of our proposed RFS-SLAM solutions in [Paper A] and [Paper B], where readers can observe the unique characteristics of RFS-SLAM.

6.4 Fusion

Now, the SLAM problem has been effectively addressed at the UE side through the utilization of RFS-SLAM, providing the UE with accurate estimations of its trajectory and a comprehensive map of the environment. However, in practice, the fusion of mapping and SLAM results from diverse sources is a common consideration. For instance, in a scenario with multiple UEs, each UE may run an individual SLAM algorithm to perceive its specific surroundings and trajectory. Additionally, different SLAM results may emerge at the same UE side, leveraging different sensors. By amalgamating information from all sensors and UEs, one anticipates achieving a more sophisticated map and more precise trajectory estimates.

Within the framework of RFS-SLAM, this fusion involves both UE state fusion and map fusion. UE state fusion is straightforward, aiming to fuse matched vectors. However, map fusion entails the fusion of RFSs, which is not a conventional approach. Nevertheless, the fused map multi-object density can be obtained by minimizing the weighted Kullback-Leibler average of multi-object densities to be fused. The resulting density is given by [114]

$$\bar{f}_k(\mathcal{X}) = \frac{\prod_{i=1}^{M} f_k^i(\mathcal{X})^{w^i}}{\int \prod_{i=1}^{M} f_k^i(\mathcal{X}')^{w^i} \delta\mathcal{X}'}, \tag{6.21}$$

where $\bar{f}_k(\mathcal{X})$ denotes the fused multi-object density, $f_k^i(\mathcal{X})$ denotes the multi-object density from i-th source with w^i representing its weight, and weights sum up to one ($\sum_{i=1}^{M} w^i = 1$). After fusion, each UE needs to update its individual maps with the fused map. It is noteworthy that the involvement of RFSs in (6.21) fundamentally distinguishes its computation from the vector-based version of (6.21). For an illustrative application example, please refer to [Paper D].

CHAPTER 7

Contributions and future work

This chapter provides an overview of the contributions made in each attached publication and delineates potential directions for future research, drawing upon the themes explored in this thesis.

7.1 Paper A

Y. Ge, F. Wen, H. Kim, M. Zhu, F. Jiang, S. Kim, L. Svensson, and H. Wymeersch, "5G SLAM using the clustering and assignment approach with diffuse multipath," in *Sensors (Basel, Switzerland)*, vol. 20, no. 16, August 2020. [Online]. Available: https://doi.org/10.3390/s20164656

In this paper, we delve into the radio SLAM problem within a 5G mmWave single BS downlink scenario, and explore the utilization of diffuse multipath in the SLAM problem. We introduce an end-to-end framework for the 5G SLAM problem, encompassing downlink data transmission, channel estimation, clustering, and the SLAM filter. A novel approach, utilizing the DBSCAN algorithm, is proposed to cluster channel measurements originating from the same source. Furthermore, we present a multi-model RBP-based PMBM-SLAM filter, aligned with the framework detailed in Section 6.3.1. The prediction and update details on the proposed SLAM filter are thoroughly provided. An innovative extended object model capable of accommodating both specular and diffuse paths is introduced, incorporating the utilization of channel gains. To assess the resulting performance of the framework, we conduct a simulation study. The results underscore the framework's efficacy in handling the radio SLAM problem, affirm the advantages of

incorporating diffuse multipath using the proposed multi-object model in SLAM, and emphasize the informative nature of channel gains for synchronizing the UE to the BS.

7.2 Paper B

Yu Ge, O. Kaltiokallio, H. Kim, F. Jiang, J. Talvitie, M. Valkama, L. Svensson, S. Kim, and H. Wymeersch, "A computationally efficient EK-PMBM filter for bistatic mmWave radio SLAM," in *IEEE Journal on Selected Areas in Communications*, vol. 40, no. 7, pp. 2179-2192, July 2022, doi: 10.1109/JSAC.2022.3155504.

In this paper, our primary focus is on mitigating the high computational cost associated with the RBP-based PMBM-SLAM filter introduced in [Paper A]. We propose low-complexity SLAM filters designed for real-time operation. Departing from the framework outlined in 6.3.1, we adopt the marginalization framework presented in 6.3.2 to address the SLAM problem. This paper introduces a novel EK-PMBM SLAM filter, employing a theoretically sound approach for the joint update of UE and landmark states through linearization using the first-order Taylor series. Additionally, we derive an algorithm to approximate the resulting PMBM to a PMB. This algorithm, based on the track-oriented marginal multi-Bernoulli/Poisson (TOMB/P) algorithm with a limited number of DAs, transforms the EK-PMBM SLAM filter into the EK-PMB SLAM filter, thus further reducing complexity. Furthermore, we extend both the EK-PMBM and EK-PMB SLAM filters to accommodate multiple landmark types, resulting in a multi-model implementation with hybrid discrete and continuous landmark states. Through simulation results utilizing realistic mmWave signal parameters, we demonstrate that the proposed filters achieve commendable mapping and positioning performance with very low complexity. Our findings also illustrate that these SLAM filters can simultaneously handle mapping and UE state estimation while accurately distinguishing the type of landmarks. The performance is comparable to that of the RBP-based PMBM-SLAM filter.

7.3 Paper C

Y. Ge, H. Khosravi, F. Jiang, H. Chen, S. Lindberg, P. Hammarberg, H. Kim, O. Brunnegård, O. Eriksson, B. Olsson, F. Tufvesson, L. Svensson, and H. Wymeersch, "Experimental validation of single BS 5G mmWave positioning and mapping for intelligent transport," submitted to *IEEE Transactions on Vehicular Technology*, 2023.

In this paper, we assess the feasibility of single BS positioning and mapping, as outlined in Section 3.3, through a real-world demonstration conforming to the current release of the 3GPP standard. The hardware specifications for the 5G single BS positioning system are introduced, encompassing the commercial BS, UE, ground-truth system, and outdoor operating environment. Special attention is given to UE and BS array configurations,

and the employed beam patterns. Technical algorithms for processing 5G mmWave measurements for positioning purposes are provided. This includes a low-complexity channel parameter estimation method for processing received measurements, a BS calibration approach, and algorithms for positioning and mapping. Specifically, we present low-complexity algorithms for single-BS LoS-only positioning using RTT and AoD, as well as mixed LoS and NLoS positioning with multipath exploitation. Additionally, a straightforward environment mapping algorithm is outlined. Positioning and mapping results are demonstrated using real 5G measurements, and performance analysis is conducted through different combinations of real and simulated measurements. Our real-life data showcases the feasibility of UE positioning with a single BS. However, the results reveal a notable performance gap between theory and practice, emphasizing the need for further improvements for enhanced performance.

7.4 Paper D

Y. Ge, H. Kim, L. Svensson, H. Wymeersch, and S. Sun, "Integrated monostatic and bistatic mmWave sensing," in *IEEE Global Communications Conference*, Kuala Lumpur, Malaysia, December 2023.

In this paper, our primary focus is on addressing the fusion problem outlined in Section 6.4 to enhance overall positioning and mapping performance. The study is conducted in a scenario where monostatic sensing is executed by the BS to map landmarks and moving objects in the environment. Concurrently, bistatic sensing is performed at the UE for SLAM. Both mapping and SLAM problems are tackled using EK-PMB (SLAM) filters from [Paper B]. To integrate UE states and maps from both monostatic and bistatic sensing, we introduce an RFS-based integration algorithm, and also provide the executable details on the proposed method. We extend the EK-PMB SLAM filter by periodically substituting the corresponding updated maps and UE states with the fused ones. Through simulations in the mmWave radio network context, we validate the advantages of integrating the two sensing modalities. The results indicate improved mapping and SLAM performances in both monostatic and bistatic sensing through periodic fusion.

7.5 Future work

This section introduces potential directions for future work based on the content of the included papers and outlines some general directions for future research.

Paper A

The current paper focuses solely on the landmark location and type; however, incorporating additional features, such as the size of the landmark, holds potential interest. Furthermore, investigating more efficient sampling methods to reduce the required num-

ber of particles is a viable consideration. Specific examples of such extensions are detailed in our papers [115,116], where different importance densities are proposed. While [Paper B] introduces a more efficient SLAM filter, the computational bottleneck persists in the estimation of parameters by rotational invariant techniques (ESPRIT) channel estimator. Designing a low-complexity ESPRIT algorithm would be an intriguing pursuit, and an example of its application in a SLAM framework can be found in our paper [117].

Paper B
This paper currently employs a point object model, but there is potential to broaden the scope by extending it into an extended object model. Additionally, applying the filter to real-world data would yield valuable insights. One direction for extension involves exploring alternative linearization methods, deviating from the current filter linearizing at the prior mean. A specific instance of this extension is presented in one of our papers [118], where the iterative posterior linearization filter is employed in lieu of the EKF.

Paper C
This study identifies several limitations that need addressing to enhance positioning and mapping performance. These include challenges such as BS calibration, synchronization errors, limited angular resolution in elevation, and a lack of comprehensive knowledge about the utilized beam patterns. Upon resolving these issues, a new phase of experimentation can be pursued. This next phase may also involve implementing optimized signal design, incorporating precoding and combining, to elevate positioning accuracy. Additionally, the extension of the scope to a SLAM problem where the UE motion model is considered, is expected to further improve the positioning accuracy.

Paper D
Currently, this paper exclusively relies on pilot signals for both monostatic and bistatic sensing. Investigating the incorporation of data in monostatic sensing would introduce a compelling dimension to the analysis. Additionally, exploring the optimal selection of fusion weights adds another intriguing avenue for further investigation.

In general, numerous promising future directions warrant exploration within the realm of mmWave radio positioning, mapping, and SLAM. One direction involves harnessing the Doppler component for enhanced analyses in positioning, mapping and SLAM, as touched upon in our paper [45, 119], with ample room for further investigations. Extending the scope of radio SLAM to address the simultaneous localization and tracking (SLAT) problem, as demonstrated in [120], where the tracking of moving objects is incorporated, constitutes another intriguing direction. Furthermore, the integration of reconfigurable intelligent surfaces (RISs) into the scenario, as exemplified in [121, 122], introduces an additional dimension for exploration.

Additionally, the exploration of multi-bounce paths offers a rich area for future work. Our existing works predominantly considers LoS paths and single-bounce paths, dismissing multi-bounce paths as disturbances to be suppressed [123]. Analyzing or harnessing

multi-bounce paths could unlock geometric information beneficial to positioning, mapping, or SLAM. Near-field scenarios offer a unique set of challenges and opportunities for investigation. The integration of deep learning techniques presents another direction to be explored. In essence, the field of mmWave radio positioning, mapping, and SLAM remains abundant with intriguing research questions and possibilities awaiting further exploration.

Bibliography

[1] T. Farley, "Mobile telephone history," *Privateline. com, http://www. privateline. com/wp-content/uploads/2016/01/TelenorPage_022-034. pdf*, 2005.

[2] J. G. Andrews, S. Buzzi, W. Choi, S. V. Hanly, A. Lozano, A. C. Soong, and J. C. Zhang, "What will 5G be?" *IEEE Journal on Selected Areas in Communications*, vol. 32, no. 6, pp. 1065–1082, 2014.

[3] M. Giordani, M. Polese, M. Mezzavilla, S. Rangan, and M. Zorzi, "Toward 6G networks: Use cases and technologies," *IEEE Communications Magazine*, vol. 58, no. 3, pp. 55–61, 2020.

[4] S. Parkvall, E. Dahlman, A. Furuskar, and M. Frenne, "NR: The new 5G radio access technology," *IEEE Communications Standards Magazine*, vol. 1, no. 4, pp. 24–30, 2017.

[5] N. Patwari, J. N. Ash, S. Kyperountas, A. O. Hero, R. L. Moses, and N. S. Correal, "Locating the nodes: Cooperative localization in wireless sensor networks," *IEEE Signal Processing Magazine*, vol. 22, no. 4, pp. 54–69, 2005.

[6] M. D. Larsen, A. L. Swindlehurst, and T. Svantesson, "Performance bounds for MIMO-OFDM channel estimation," *IEEE Transactions on Signal Processing*, vol. 57, no. 5, pp. 1901–1916, 2009.

[7] A. Shahmansoori, G. E. Garcia, G. Destino, G. Seco-Granados, and H. Wymeersch, "Position and orientation estimation through millimeter-wave MIMO in 5G systems," *IEEE Transactions on Wireless Communications*, vol. 17, no. 3, pp. 1822–1835, 2017.

[8] H. Wymeersch, N. Garcia, H. Kim, G. Seco-Granados, S. Kim, F. Wen, and M. Fröhle, "5G mm wave downlink vehicular positioning," in *IEEE Global Communications Conference (GLOBECOM)*, 2018, pp. 206–212.

[9] E. Leitinger, F. Meyer, F. Hlawatsch, K. Witrisal, F. Tufvesson, and M. Z. Win, "A belief propagation algorithm for multipath-based SLAM," *IEEE Transactions on Wireless Communication*, vol. 18, no. 12, pp. 5613–5629, Sep. 2019.

[10] Y. Ge, O. Kaltiokallio, H. Kim, J. Talvitie, S. Kim, L. Svensson, M. Valkama, and H. Wymeersch, "Mmwave mapping and SLAM for 5G and beyond," in *Integrated Sensing and Communications*. Springer, 2023, pp. 445–475.

[11] T. G. Reid, S. E. Houts, R. Cammarata, G. Mills, S. Agarwal, A. Vora, and G. Pandey, "Localization requirements for autonomous vehicles," *arXiv preprint arXiv:1906.01061*, 2019.

[12] S.-W. Ko, H. Chae, K. Han, S. Lee, D.-W. Seo, and K. Huang, "V2X-based vehicular positioning: Opportunities, challenges, and future directions," *IEEE Wireless Communications*, vol. 28, no. 2, pp. 144–151, 2021.

[13] Z. Zhang, S.-W. Ko, R. Wang, and K. Huang, "Cooperative multi-point vehicular positioning using millimeter-wave surface reflection," *IEEE Transactions on Wireless Communications*, vol. 20, no. 4, pp. 2221–2236, 2020.

[14] H. Guo, B. Makki, D.-T. Phan-Huy, E. Dahlman, M.-S. Alouini, and T. Svensson, "Predictor antenna: A technique to boost the performance of moving relays," *IEEE Communications Magazine*, vol. 59, no. 7, pp. 80–86, 2021.

[15] M. Furkan Keskin, F. Jiang, F. Munier, G. Seco-Granados, and H. Wymeersch, "Optimal spatial signal design for mmWave positioning under imperfect synchronization," *IEEE Transactions on Vehicular Technology*, vol. 71, no. 5, pp. 5558–5563, 2022.

[16] N. C. Luong, X. Lu, D. T. Hoang, D. Niyato, and D. I. Kim, "Radio resource management in joint radar and communication: A comprehensive survey," *IEEE Communications Surveys & Tutorials*, 2021.

[17] P. Kumari, A. Mezghani, and R. W. Heath, "JCR70: A low-complexity millimeter-wave proof-of-concept platform for a fully-digital SIMO joint communication-radar," *IEEE Open Journal of Vehicular Technology*, 2021.

[18] L. Han and K. Wu, "24-GHz integrated radio and radar system capable of time-agile wireless communication and sensing," *IEEE Transactions on Microwave Theory and Techniques*, vol. 60, no. 3, pp. 619–631, 2012.

[19] H. Guo, B. Makki, M.-S. Alouini, and T. Svensson, "High-rate uninterrupted internet of vehicle communications in highways: Dynamic blockage avoidance and CSIT acquisition," *IEEE Communications Magazine*, vol. 60, no. 7, pp. 44–50, 2022.

[20] J. A. del Peral-Rosado, R. Raulefs, J. A. López-Salcedo, and G. Seco-Granados, "Survey of cellular mobile radio localization methods: From 1G to 5G," *IEEE Communications Surveys & Tutorials*, vol. 20, no. 2, pp. 1124–1148, 2017.

[21] H. Wymeersch, G. Seco-Granados, G. Destino, D. Dardari, and F. Tufvesson, "5G mmWave positioning for vehicular networks," *IEEE Wireless Communications*, vol. 24, no. 6, pp. 80–86, 2017.

[22] N. Joubert, T. G. Reid, and F. Noble, "Developments in modern GNSS and its impact on autonomous vehicle architectures," in *IEEE Intelligent Vehicles Symposium (IV)*, 2020, pp. 2029–2036.

[23] E. Javanmardi, M. Javanmardi, Y. Gu, and S. Kamijo, "Factors to evaluate capability of map for vehicle localization," *IEEE Access*, vol. 6, pp. 49 850–49 867, 2018.

[24] J. Einsiedler, I. Radusch, and K. Wolter, "Vehicle indoor positioning: A survey," in *14th Workshop on Positioning, Navigation and Communications (WPNC)*, 2017, pp. 1–6.

[25] V. Ilci and C. Toth, "High definition 3D map creation using GNSS/IMU/LiDAR sensor integration to support autonomous vehicle navigation," *Sensors*, vol. 20, no. 3, p. 899, 2020.

[26] S. Dwivedi, R. Shreevastav, F. Munier, J. Nygren, I. Siomina, Y. Lyazidi, D. Shrestha, G. Lindmark, P. Ernström, E. Stare *et al.*, "Positioning in 5G networks," *IEEE Communications Magazine*, vol. 59, no. 11, pp. 38–44, 2021.

[27] 3GPP, "Study on NR positioning support," TR 38.855, Technical Report 16.0.0, 2019.

[28] ——, "Study on scenarios and requirements of in-coverage, partial coverage, and out-of-coverage NR positioning use cases," TR 38.845, Technical Report 17.0.0, 2021.

[29] ——, "Study on expanded and improved NR positioning," TR 38.859, Technical Report 0.1.0, 2022.

[30] R. Keating, M. Säily, J. Hulkkonen, and J. Karjalainen, "Overview of positioning in 5G new radio," in *16th International Symposium on Wireless Communication Systems (ISWCS)*, 2019, pp. 320–324.

[31] J. A. del Peral-Rosado, J. A. López-Salcedo, S. Kim, and G. Seco-Granados, "Feasibility study of 5G-based localization for assisted driving," in *International Conference on Localization and GNSS (ICL-GNSS)*, 2016, pp. 1–6.

[32] M. Posluk, J. Ahlander, D. Shrestha, S. M. Razavi, G. Lindmark, and F. Gunnarsson, "5G deployment strategies for high positioning accuracy in indoor environments," *arXiv preprint arXiv:2105.09584*, 2021.

[33] K. Witrisal, P. Meissner, E. Leitinger, Y. Shen, C. Gustafson, F. Tufvesson, K. Haneda, D. Dardari, A. F. Molisch, A. Conti *et al.*, "High-accuracy localization

for assisted living: 5G systems will turn multipath channels from foe to friend," *IEEE Signal Processing Magazine*, vol. 33, no. 2, pp. 59–70, 2016.

[34] F. Wen, J. Kulmer, K. Witrisal, and H. Wymeersch, "5G positioning and mapping with diffuse multipath," *IEEE Transactions on Wireless Communications*, 2020.

[35] R. Mendrzik, H. Wymeersch, G. Bauch, and Z. Abu-Shaban, "Harnessing NLOS components for position and orientation estimation in 5G millimeter wave MIMO," *IEEE Transactions on Wireless Communications*, vol. 18, no. 1, pp. 93–107, 2019.

[36] F. Mata, F. Grec, M. Azaola, F. Blázquez, A. Fernández, E. Dominguez, G. Cueto-Felgueroso, G. Seco-Granados, J. del Peral-Rosado, E. Staudinger *et al.*, "Preliminary field trials and simulations results on performance of hybrid positioning based on GNSS and 5G signals," in *Proceedings of the 33rd International Technical Meeting of the Satellite Division of The Institute of Navigation (ION GNSS+)*, 2020, pp. 387–401.

[37] G. Yammine, M. Alawieh, G. Ilin, M. Momani, M. Elkhouly, P. Karbownik, N. Franke, and E. Eberlein, "Experimental investigation of 5G positioning performance using a mmWave measurement setup," in *International Conference on Indoor Positioning and Indoor Navigation (IPIN)*, 2021, pp. 1–8.

[38] Y. Ge, H. Chen, F. Jiang, M. Zhu, H. Khosravi, S. Lindberg, H. Herbertsson, O. Eriksson, O. Brunnegård, B.-E. Olsson *et al.*, "Experimental validation of single base station 5G mmWave positioning: Initial findings," in *25th International Conference on Information Fusion (FUSION)*, 2022, pp. 1–8.

[39] J. del Peral-Rosado, G. Granados, R. Raulefs, E. Leitinger, S. Grebien, T. Wilding, D. Dardari, E. Lohan, H. Wymeersch, J. Floch *et al.*, "White paper on new localization methods for 5G wireless systems and the internet-of-things," *COST Action CA15104*, 2018.

[40] H. Durrant-Whyte and T. Bailey, "Simultaneous localization and mapping: Part I," *IEEE Robotics & Automation Magazine*, vol. 13, no. 2, pp. 99–110, 2006.

[41] T. Bailey and H. Durrant-Whyte, "Simultaneous localization and mapping (SLAM): Part II," *IEEE Robotics & Automation Magazine*, vol. 13, no. 3, pp. 108–117, 2006.

[42] J. Talvitie, M. Valkama, G. Destino, and H. Wymeersch, "Novel algorithms for high-accuracy joint position and orientation stimation in 5G mmWave systems," in *IEEE Globecom Workshops (GC Workshops)*, 2017.

[43] R. Mendrzik, H. Wymeersch, and G. Bauch, "Joint localization and mapping through millimeter wave MIMO in 5G systems," in *IEEE Global Communications Conference (GLOBECOM)*, 2018, pp. 1–6.

[44] A. Fascista, A. Coluccia, H. Wymeersch, and G. Seco-Granados, "Downlink single-snapshot localization and mapping with a single-antenna receiver," *IEEE Transactions on Wireless Communications*, vol. 20, no. 7, pp. 4672–4684, 2021.

[45] H. Chen, F. Jiang, Y. Ge, H. Kim, and H. Wymeersch, "Doppler-enabled single-antenna localization and mapping without synchronization," in *IEEE Global Communications Conference (GLOBECOM)*, 2022, pp. 6469–6474.

[46] R. P. Mahler, ""Statistics 101" for multisensor, multitarget data fusion," *IEEE Aerospace and Electronic Systems Magazine*, vol. 19, no. 1, pp. 53–64, 2004.

[47] F. Meyer, P. Braca, P. Willett, and F. Hlawatsch, "A scalable algorithm for tracking an unknown number of targets using multiple sensors," *IEEE Transactions on Signal Processing*, vol. 65, no. 13, pp. 3478–3493, 2017.

[48] F. Meyer, T. Kropfreiter, J. L. Williams, R. Lau, F. Hlawatsch, P. Braca, and M. Z. Win, "Message passing algorithms for scalable multitarget tracking," *Proceedings of the IEEE*, vol. 106, no. 2, pp. 221–259, 2018.

[49] R. P. Mahler, *Advances in Statistical Multisource-Multitarget Information Fusion*. Artech House, 2014.

[50] R. Mahler, "PHD filters for nonstandard targets, I: Extended targets," in *International Conference on Information Fusion*. IEEE, 2009, pp. 915–921.

[51] Á. F. García-Fernández, J. L. Williams, K. Granström, and L. Svensson, "Poisson multi-Bernoulli mixture filter: Direct derivation and implementation," *IEEE Transactions on Aerospace and Electronic Systems*, vol. 54, no. 4, pp. 1883–1901, 2018.

[52] J.-L. Blanco, "A tutorial on SE (3) transformation parameterizations and on-manifold optimization," *University of Malaga, Tech. Rep*, vol. 3, p. 6, 2010.

[53] J. Palacios, G. Bielsa, P. Casari, and J. Widmer, "Single-and multiple-access point indoor localization for millimeter-wave networks," *IEEE Transactions on Wireless Communications*, vol. 18, no. 3, pp. 1927–1942, 2019.

[54] A. Richter, "Estimation of radio channel parameters: Models and algorithms," Ph.D. dissertation, Ilmenau University of Technology, 2005.

[55] K. Venugopal, A. Alkhateeb, N. G. Prelcic, and R. W. Heath, "Channel estimation for hybrid architecture-based wideband millimeter wave systems," *IEEE Journal on Selected Areas in Communications*, vol. 35, no. 9, pp. 1996–2009, 2017.

[56] A. B. Gershman, M. Rübsamen, and M. Pesavento, "One- and two-dimensional direction-of-arrival estimation: An overview of search-free techniques," *Signal Processing*, vol. 90, no. 5, pp. 1338 – 1349, 2010.

[57] F. Jiang, F. Wen, Y. Ge, M. Zhu, H. Wymeersch, and F. Tufvesson, "Beamspace multidimensional ESPRIT approaches for simultaneous localization and communications," *arXiv preprint arXiv:2111.07450*, 2021.

[58] F. Jiang, Y. Ge, M. Zhu, H. Wymeersch, and F. Tufvesson, "Low-complexity channel estimation and localization with random beamspace observations," in *IEEE International Conference on Communications*, 2023, pp. 5985–5990.

[59] M. Koivisto, A. Hakkarainen, M. Costa, P. Kela, K. Leppanen, and M. Valkama, "High-efficiency device positioning and location-aware communications in dense 5G networks," *IEEE Communications Magazine*, vol. 55, no. 8, pp. 188–195, 2017.

[60] F. Wen and H. Wymeersch, "5G synchronization, positioning, and mapping from diffuse multipath," *IEEE Wireless Communications Letters*, vol. 10, no. 1, pp. 43–47, 2020.

[61] M. A. Nazari, G. Seco-Granados, P. Johannisson, and H. Wymeersch, "Mmwave 6D radio localization with a snapshot observation from a single BS," *IEEE Transactions on Vehicular Technology*, 2023.

[62] F. Guidi, A. Guerra, and D. Dardari, "Personal mobile radars with millimeter-wave massive arrays for indoor mapping," *IEEE Transactions on Mobile Computing*, vol. 15, no. 6, pp. 1471–1484, 2015.

[63] E. Ahvar, N. Daneshgar-Moghaddam, A. M. Ortiz, G. M. Lee, and N. Crespi, "On analyzing user location discovery methods in smart homes: A taxonomy and survey," *Journal of Network and Computer Applications*, vol. 76, pp. 75–86, 2016.

[64] R. D. Taranto, S. Muppirisetty, R. Raulefs, D. Slock, T. Svensson, and H. Wymeersch, "Location-aware communications for 5G networks," *IEEE Signal Processing Magazine*, vol. 31, no. 6, pp. 102–112, Nov 2014.

[65] A. Yaeli, P. Bak, G. Feigenblat, S. Nadler, H. Roitman, G. Saadoun, H. J. Ship, D. Cohen, O. Fuchs, S. Ofek-Koifman *et al.*, "Understanding customer behavior using indoor location analysis and visualization," *IBM Journal of Research and Development*, vol. 58, no. 5/6, pp. 3–1, 2014.

[66] R. S. Campos *et al.*, "Evolution of positioning techniques in cellular networks, from 2G to 4G," *Wireless Communications and Mobile Computing*, vol. 2017, 2017.

[67] D. D. McCrady, L. Doyle, H. Forstrom, T. Dempsey, and M. Martorana, "Mobile ranging using low-accuracy clocks," *IEEE Transactions on Microwave Theory and Techniques*, vol. 48, no. 6, pp. 951–958, 2000.

[68] S. Kim, T. Pals, R. A. Iltis, and H. Lee, "Cdma multipath channel estimation using generalized successive interference cancellation algorithm for radiolocation," in *37th Annual Conference on Information Sciences and Systems*. Citeseer, 2002.

[69] Y. Ge, M. Stark, M. F. Keskin, F. Hofmann, T. Hansen, and H. Wymeersch, "Analysis of V2X sidelink positioning in sub-6 GHz," in *IEEE 3rd International Symposium on Joint Communications & Sensing (JC&S)*, 2023, pp. 1–6.

[70] J. F. Bull, "Wireless geolocation," *IEEE Vehicular Technology Magazine*, vol. 4, no. 4, pp. 45–53, 2009.

[71] S. S. Cherian and A. N. Rudrapatna, "LTE location technologies and delivery solutions," *Bell Labs Technical Journal*, vol. 18, no. 2, pp. 175–194, 2013.

[72] E. R. Robinson and A. H. Quazi, "Effect of sound-speed profile on differential time-delay estimation," *The Journal of the Acoustical Society of America*, vol. 77, no. 3, pp. 1086–1090, 1985.

[73] J. J. Caffery and G. L. Stuber, "Radio location in urban cdma microcells," in *Proceedings of 6th International Symposium on Personal, Indoor and Mobile Radio Communications*, vol. 2, 1995, pp. 858–862.

[74] Y. Shen and M. Z. Win, "Fundamental limits of wideband localization—Part I: A general framework," *IEEE Transactions on Information Theory*, vol. 56, no. 10, pp. 4956–4980, 2010.

[75] J. Ash and L. Potter, "Sensor network localization via received signal strength measurements with directional antennas," in *Proceedings of the Allerton Conference on Communication, Control, and Computing*, 2004, pp. 1861–1870.

[76] Y. Liu, X. Shi, S. He, and Z. Shi, "Prospective positioning architecture and technologies in 5G networks," *IEEE Network*, vol. 31, no. 6, pp. 115–121, 2017.

[77] M. Ester, H.-P. Kriegel, J. Sander, X. Xu *et al.*, "A density-based algorithm for discovering clusters in large spatial databases with noise," in *International Conference on Knowledge Discovery and Data Mining*, 1996, pp. 226–231.

[78] H. Kim, K. Granström, L. Gao, G. Battistelli, S. Kim, and H. Wymeersch, "5G mmWave cooperative positioning and mapping using multi-model PHD filter and map fusion," *IEEE Transactions on Wireless Communications*, 2020.

[79] M. Montemerlo, S. Thrun, D. Koller, and B. Wegbreit, "FastSLAM: A factored solution to the simultaneous localization and mapping problem," in *Eighteenth National Conference on Artificial Intelligence*. USA: American Association for Artificial Intelligence, 2002, p. 593–598.

[80] S. Särkkä and L. Svensson, *Bayesian filtering and smoothing*. Cambridge university press, 2023, vol. 17.

[81] M. Dissanayake, P. Newman, S. Clark, H. Durrant-Whyte, and M. Csorba, "A solution to the simultaneous localization and map building (SLAM) problem," *IEEE Transactions on Robotics and Automation*, vol. 17, no. 3, pp. 229–241, 2001.

[82] J. Neira and J. Tardos, "Data association in stochastic mapping using the joint compatibility test," *IEEE Transactions on Robotics and Automation*, vol. 17, no. 6, pp. 890–897, 2001.

[83] G. Grisetti, R. Kümmerle, C. Stachniss, and W. Burgard, "A tutorial on graph-based SLAM," *IEEE Intelligent Transportation Systems Magazine*, vol. 2, no. 4, pp. 31–43, 2010.

[84] S. Thrun and M. Montemerlo, "The graph SLAM algorithm with applications to large-scale mapping of urban structures," *The International Journal of Robotics Research*, vol. 25, no. 5-6, pp. 403–429, 2006.

[85] E. Olson, J. Leonard, and S. Teller, "Fast iterative alignment of pose graphs with poor initial estimates," in *Proceedings IEEE International Conference on Robotics and Automation.*, 2006, pp. 2262–2269.

[86] G. Grisetti, C. Stachniss, and W. Burgard, "Nonlinear constraint network optimization for efficient map learning," *IEEE Transactions on Intelligent Transportation Systems*, vol. 10, no. 3, pp. 428–439, 2009.

[87] F. R. Kschischang, B. J. Frey, and H.-A. Loeliger, "Factor graphs and the sum-product algorithm," *IEEE Transactions on Information Theory*, vol. 47, no. 2, pp. 498–519, Feb. 2001.

[88] R. Mendrzik, F. Meyer, G. Bauch, and M. Z. Win, "Enabling situational awareness in millimeter wave massive MIMO systems," *IEEE Journal of Selected Topics in Signal Processing*, vol. 13, no. 5, pp. 1196–1211, Aug. 2019.

[89] E. Leitinger, S. Grebien, and K. Witrisal, "Multipath-based SLAM exploiting AoA and amplitude information," in *International Conference on Communications Workshops (ICC Workshops)*, Shanghai, China, May 2019, pp. 1–7.

[90] R. Mendrzik, F. Meyer, G. Bauch, and M. Win, "Localization, mapping, and synchronization in 5G millimeter wave massive MIMO systems," in *IEEE 20th International Workshop on Signal Processing Advances in Wireless Communications (SPAWC)*, 2019, pp. 1–5.

[91] J. Mullane, B.-N. Vo, M. D. Adams, and B.-T. Vo, "A random-finite-set approach to Bayesian SLAM," *IEEE Transactions on Robotics*, vol. 27, no. 2, pp. 268–282, 2011.

[92] H. Deusch, S. Reuter, and K. Dietmayer, "The labeled multi-Bernoulli SLAM filter," *IEEE Signal Processing Letters*, vol. 22, no. 10, pp. 1561–1565, 2015.

[93] H. Deusch, "Random finite set-based localization and SLAM for highly automated vehicles," Ph.D. dissertation, Universität Ulm, 2016.

[94] D. Moratuwage, M. Adams, and F. Inostroza, "δ-generalised labelled multi-Bernoulli simultaneous localisation and mapping," in *International Conference on Control, Automation and Information Sciences (ICCAIS)*, 2018, pp. 175–182.

[95] ——, "δ-generalized labeled multi-Bernoulli simultaneous localization and mapping with an optimal kernel-based particle filtering approach," *Sensors*, vol. 19, no. 10, p. 2290, 2019.

[96] O. Kaltiokallio, Y. Ge, J. Talvitie, H. Wymeersch, and M. Valkama, "mmWave simultaneous localization and mapping using a computationally efficient EK-PHD filter," in *IEEE International Conference on Information Fusion (Fusion)*, 2021, pp. 1–6.

[97] Y. Ge, H. Kim, F. Wen, L. Svensson, S. Kim, and H. Wymeersch, "Exploiting diffuse multipath in 5G SLAM," in *IEEE Global Communications Conference*, 2020, pp. 1–6.

[98] Y. Ge, F. Wen, H. Kim, M. Zhu, F. Jiang, S. Kim, L. Svensson, and H. Wymeersch, "5G SLAM using the clustering and assignment approach with diffuse multipath," *Sensors (Basel, Switzerland)*, vol. 20, no. 16, August 2020. [Online]. Available: https://doi.org/10.3390/s20164656

[99] Y. Ge, O. Kaltiokallio, H. Kim, F. Jiang, J. Talvitie, M. Valkama, L. Svensson, S. Kim, and H. Wymeersch, "A computationally efficient EK-PMBM filter for bistatic mmWave radio SLAM," *IEEE Journal on Selected Areas in Communications*, 2022.

[100] H. Kim, K. Granström, L. Svensson, S. Kim, and H. Wymeersch, "PMBM-based SLAM filters in 5G mmwave vehicular networks," *IEEE Transactions on Vehicular Technology*, vol. 71, no. 8, pp. 8646–8661, 2022.

[101] Y. Ge, H. Kim, L. Svensson, H. Wymeersch, and S. Sun, "Integrated monostatic and bistatic mmWave sensing," *arXiv preprint arXiv:2308.13729*, 2023.

[102] R. Mahler, *Statistical Multisource-Multitarget Information Fusion.* Artech House, 2007.

[103] J. L. Williams, "Marginal multi-Bernoulli filters: RFS derivation of MHT, JIPDA, and association-based MeMBer," *IEEE Transactions on Aerospace and Electronic Systems*, vol. 51, no. 3, pp. 1664–1687, 2015.

[104] Á. F. García-Fernández, J. L. Williams, L. Svensson, and Y. Xia, "A Poisson multi-Bernoulli mixture filter for coexisting point and extended targets," *IEEE Transactions on Signal Processing*, vol. 69, pp. 2600–2610, 2021.

[105] D. Schuhmacher and A. Xia, "A new metric between distributions of point processes," *Advances in Applied Probability*, vol. 40, no. 3, pp. 651–672, 2008.

[106] D. Schuhmacher, B.-T. Vo, and B.-N. Vo, "A consistent metric for performance evaluation of multi-object filters," *IEEE Transactions on Signal Processing*, vol. 56, no. 8, pp. 3447–3457, 2008.

[107] A. S. Rahmathullah, Á. F. García-Fernández, and L. Svensson, "Generalized optimal sub-pattern assignment metric," in *International Conference on Information Fusion (Fusion)*, 2017, pp. 1–8.

[108] Á. F. García-Femández and L. Svensson, "Spooky effect in optimal OSPA estimation and how GOSPA solves it," in *International Conference on Information Fusion (FUSION)*, 2019, pp. 1–8.

[109] K. Granström, M. Fatemi, and L. Svensson, "Poisson multi-Bernoulli mixture conjugate prior for multiple extended target filtering," *IEEE Transactions on Aerospace and Electronic Systems*, vol. 56, no. 1, pp. 208–225, 2019.

[110] S. Särkkä, *Bayesian Filtering and Smoothing*. Cambridge University Press, 2013.

[111] J. S. Liu and J. S. Liu, *Monte Carlo strategies in scientific computing*. Springer, 2001, vol. 75.

[112] R. P. Mahler, "Multitarget Bayes filtering via first-order multitarget moments," *IEEE Transactions on Aerospace and Electronic systems*, vol. 39, no. 4, pp. 1152–1178, 2003.

[113] N. Chopin, O. Papaspiliopoulos *et al.*, *An introduction to sequential Monte Carlo*. Springer, 2020, vol. 4.

[114] G. Battistelli, L. Chisci, C. Fantacci, A. Farina, and A. Graziano, "Consensus CPHD filter for distributed multitarget tracking," *IEEE Journal of Selected Topics in Signal Processing*, vol. 7, no. 3, pp. 508–520, 2013.

[115] O. Kaltiokallio, R. Hostettler, J. Talvitie, Y. Ge, H. Kim, H. Wymeersch, and M. Valkama, "Towards real-time radio-SLAM via optimal importance sampling," in *IEEE 23rd International Workshop on Signal Processing Advances in Wireless Communication (SPAWC)*, 2022, pp. 1–5.

[116] O. Kaltiokallio, R. Hostettler, Y. Ge, H. Kim, J. Talvitie, H. Wymeersch, and M. Valkama, "A multi-hypotheses importance density for SLAM in cluttered scenarios," *IEEE Transactions on Robotics*, 2023.

[117] Y. Ge, F. Jiang, M. Zhu, F. Wen, L. Svensson, and H. Wymeersch, "5G SLAM with low-complexity channel estimation," in *IEEE 15th European Conference on Antennas and Propagation (EuCAP)*, 2021, pp. 1–5.

[118] Y. Ge, Y. Wu, F. Jiang, O. Kaltiokallio, J. Talvitie, M. Valkama, L. Svensson, and H. Wymeersch, "Iterated posterior linearization PMB filter for 5G SLAM," in *IEEE International Conference on Communications*, 2022, pp. 877–882.

[119] Y. Ge, O. Kaltiokallio, H. Chen, F. Jiang, J. Talvitie, M. Valkama, L. Svensson, and H. Wymeersch, "Doppler exploitation in bistatic mmWave radio SLAM," in *IEEE Global Communications Conference*, 2022, pp. 6463–6468.

[120] H. Kim, J. Lee, Y. Ge, F. Jiang, S. Kim, and H. Wymeersch, "Cooperative mmWave PHD-SLAM with moving scatterers," in *International Conference on Information Fusion (FUSION)*, 2022, pp. 1–6.

[121] H. Kim, A. Fascista, H. Chen, Y. Ge, G. C. Alexandropoulos, G. Seco-Granados, and H. Wymeersch, "RIS-aided monostatic sensing and object detection with single and double bounce multipath," in *IEEE International Conference on Communications Workshops (ICC Workshops)*, 2023, pp. 1883–1889.

[122] H. Kim, H. Chen, M. F. Keskin, Y. Ge, K. Keykhosravi, G. C. Alexandropoulos, S. Kim, and H. Wymeersch, "RIS-enabled and access-point-free simultaneous radio localization and mapping," *IEEE Transactions on Wireless Communications*, 2023.

[123] O. Kaltiokallio, J. Talvitie, Y. Ge, H. Wymeersch, and M. Valkama, "mmWave mapping using PHD with smoothed track confirmation and multi-bounce suppression," in *IEEE International Conference on Communications Workshops (ICC Workshops)*, 2022, pp. 67–72.